Astronomy & Astrophysics manuscript no. ms˙ref˙report˙3
August 30, 2016
© ESO 2016

arXiv:1608.07661v1 [astro-ph.SR] 27 Aug 2016

The evolutionary status of dense cores in the NGC 1333 IRAS 4 star-forming region

E. Koumpia[1,2,9], F.F.S. van der Tak[1,2], W. Kwon[3,8], J.J. Tobin[4,5], G.A. Fuller[6], R. Plume[7]

[1] SRON Netherlands Institute for Space Research, Landleven 12, 9747 AD Groningen, The Netherlands
[2] Kapteyn Institute, University of Groningen, Landleven 12, 9747 AD Groningen, The Netherlands
[3] Korea Astronomy and Space Science Institute, 776, Daedeok-Daero, Yuseong-gu, Daejeon, 34055, Korea
[4] National Radio Astronomy Observatory, Charlottesville, VA 22903, USA
[5] Leiden Observatory, Leiden University, P.O. Box 9513, 2300-RA Leiden, The Netherlands
[6] Jodrell Bank Centre for Astrophysics & UK ALMA Regional Centre Node, School of Physics & Astronomy, The University of Manchester, Manchester, M13 9PL, UK
[7] Department of Physics & Astronomy and Institute for Space Imaging Sciences, University of Calgary, Calgary, AB T2N 1N4, Canada
[8] Korea University of Science and Technology, 217 Gajeong-ro, Yuseong-gu, Daejeon 34113, Korea
[9] e-mail: ev.koumpia@gmail.com

Received date/Accepted date

ABSTRACT

Context. Protostellar evolution, following the formation of the protostar is becoming reasonably well characterized, but the evolution from a prestellar core to a protostar is not well known, although the first hydrostatic core (FHSC) must be a pivotal step.
Aims. NGC 1333 – IRAS 4C is a potentially very young object, that we can directly compare with the nearby Class 0 objects IRAS 4A and IRAS 4B. Observational constraints are provided by spectral imaging from the JCMT Spectral Legacy Survey (330–373 GHz). We present integrated intensity and velocity maps of several species, including CO, H_2CO and CH_3OH. CARMA observations provide us with additional information to distinguish IRAS 4C from other evolutionary stages.
Methods. The velocity of an observed outflow, the degree of CO depletion, the deuterium fractionation of $[DCO^+]/[HCO^+]$ and gas kinetic temperatures are observational signatures that we present.
Results. We report differences between the three sources in four aspects: a) the kinetic temperature as probed using the H_2CO lines is much lower towards IRAS 4C than the other two sources, b) the line profiles of the detected species show strong outflow activity towards IRAS 4A and IRAS 4B but not towards IRAS 4C, c) the HCN/HNC is < 1 towards IRAS 4C, which confirms the cold nature of the source, d) the degree of CO depletion and the deuteration are the lowest towards the warmest of the sources, IRAS 4B.
Conclusions. IRAS 4C seems to be in a different evolutionary state than the IRAS 4A and IRAS 4B sources. We can probably exclude the FHSC stage due to the relatively low L_{smm}/L_{bol} (~6 %) and we investigate the earliest accretion phase of Class 0 stage and the transition between Class 0 to Class I. Our results do not show a consistent scenario for either case, with the major issue being the absence of outflow activity and the cold nature of IRAS 4C. The number of FHSC candidates in Perseus is ~10 times higher than current models predict, which suggests that the lifespan of these objects is $\geq 10^3$ years, possibly due to an accretion rate lower than 4×10^{-5} $M_\odot$/yr.

Key words. ISM: individual (NGC 1333), ISM: kinematics and dynamics, ISM: molecules, stars: formation

1. Introduction

Stars form by gravitational collapse of dense cores in molecular clouds. In order to understand the origin of stellar masses, multiple systems and outflows, it is necessary to understand the formation and evolution of dense cores. Representing the earliest phase of star formation, both prestellar and protostellar cores have been observed and studied using large (sub–) millimeter telescopes (e.g. JCMT; Enoch et al. 2006; van Kempen et al. 2006), infrared (e.g. Spitzer; Evans et al. 2003, 2009; Jørgensen et al. 2006; Hatchell et al. 2005; Young et al. 2004) and interferometers (e.g. CARMA; Enoch et al. 2010; Di Francesco et al. 2001). While the basic evolutionary ordering of protostellar objects seems firmly established (e.g.; Andre et al. 2000), we still do not have a clear view of the evolutionary process that turns a prestellar core into a protostar (Bergin & Tafalla 2007; Evans et al. 2009).

The transition from pre–stellar to protostellar cores is predicted to be the first hydrostatic core, FHSC (Larson 1969), which represents the phase after the collapse of the parent core and before the formation of a protostar. This object is characterized by a very short lifetime (~1000 years; Machida et al. 2008). Recent studies have provided a few candidates including Per–bolo 58, L1448–IRS2E, LDN 1451–mm, B1–bN, B1–bS and Per–bolo 45(Enoch et al. 2010; Chen et al. 2010; Pineda et al. 2011; Pezzuto et al. 2012; Schnee et al. 2012). Statistically, using

$$N_{FHSC} = N_{CLASS0}\frac{\tau_{FHSC}}{\tau_{CLASS0}} \quad (1)$$

and assuming a lifespan of $\sim10^3$ yrs for FHSC and $2.2\sim10^5$ yrs for Class 0 objects (Enoch et al. 2009), while there are about 27 Class 0 objects in Perseus (Enoch et al. 2009), the predicted number of FHSC in Perseus is ≤ 0.2. When adopting a lifetime of $\sim10^4$ yr for Class 0 objects based on outflow kinematic

timescale (Machida & Hosokawa 2013), the predicted number of FHSC in Perseus is about 5, which is closer to the observed number.

Another very early stage of low–mass star formation is the very low luminosity object (VeLLO) which is characterized by an internal luminosity of $\leq 0.1 L_{\odot}$. Dunham et al. (2008) report 15 VeLLO candidates, while even fewer have been studied in detail (e.g. L1014–IRS, L1521F–IR, IRAM 04191+1522; Young et al. 2004; Bourke et al. 2006; Dunham et al. 2006). VeLLOs have been associated with a brown dwarf progenitor (Lee et al. 2013) or a very low mass Class 0 protostar with low accretion, but their exact nature is still uncertain.

The NGC 1333 region in the Perseus molecular cloud is an excellent laboratory to study early stages of low–mass star formation. NGC 1333 is a nearby (D=235 pc; Hirota et al. 2008) and young (< 1 My; Gutermuth et al. 2008) star forming region. It is a part of the Perseus OB2 molecular cloud complex which contains a large number of young stellar objects (YSOs). It hosts about 50 YSOs and 36 Herbig–Haro objects.

This work focuses on three YSOs in NGC 1333: IRAS 4A, IRAS 4B and IRAS 4C. While IRAS 4A and IRAS 4B are well studied Class 0 objects, the nature of IRAS 4C is still under debate. Previous studies, including Enoch et al. (2009) and Sadavoy et al. (2014) classified IRAS 4C also as a Class 0 YSO. Both IRAS 4A and IRAS 4B are found to be binaries. Sandell & Knee (2001) and Di Francesco et al. (2001) resolved the IRAS 4B/IRAS 4B II binary using JCMT and PdBI reporting the fainter binary companion IRAS 4B II at ∼10 ″ to the east of IRAS 4B. IRAS 4B II has been called IRAS 4C as well (e.g.; Looney et al. 2000) but IRAS 4C is generally used as the source in our work which is ∼40″ east–northeast of IRAS 4A (e.g.; Smith et al. 2000).

Interferometric observations of ammonia towards all three sources were briefly reported in Wootten (1995), where only the emission from IRAS 4A was clearly associated with outflowing warm gas. In the same study IRAS 4C does not show that clear association with the structures located near the protostellar environment. Interferometric observations of ammonia and of NH_2D towards IRAS 4A and IRAS 4C were reported in Shah & Wootten (2001) and indicated colder conditions towards IRAS 4C.

This paper uses JCMT (James Clerk Maxwell Telescope) molecular line emission and CARMA (Combined Array for Research in Millimeter-wave Astronomy) dust continuum observations to clarify the evolutionary status of IRAS 4C, using the nearby IRAS 4A and IRAS 4B sources as comparison standards and study the physical and chemical structure that characterizes these very early evolutionary stages. Our study of IRAS 4C is unique since it provides information about the spatial and velocity structure of many molecules while it has previously been studied mainly photometrically (e.g.; Dunham et al. 2008; Enoch et al. 2009; Sadavoy et al. 2014).

In order to understand the nature of IRAS 4C, it is crucial to obtain the properties of the dust and gas that are present in its envelope and outflow. One of the observational signatures that distinguish a FHSC from a typical protostar is the velocity of the molecular outflow. According to models, a FHSC should be able to drive an early outflow which is expected to be weak and of low velocity V ∼ 3 km s^{-1} (Machida et al. 2008; Tomida et al. 2010), while the typical speed of a protostellar outflow is 10–20 km s^{-1} (Arce & Sargent 2006). Thus, measuring the velocity of an observed outflow could test the evolutionary stage of IRAS 4C. Water masers could indicate an outflow activity but several interferometric surveys have not detected associated maser emission near IRAS 4C (Rodríguez et al. 2002; Furuya et al. 2003; Park & Choi 2007).

Another observational tool is the deuterium fractionation (e.g. $[N_2D^+]/[N_2H^+]$), which can be used as a chemical clock (Belloche et al. 2006; Fontani et al. 2011, 2014). Deuterated species are enhanced in environments of low temperatures (T< 20 K) where CO is depleted (Millar et al. 1989). The coldest (i.e. the youngest) objects are characterised by the largest deuterium fractionation (Crapsi et al. 2005a).

Although there is not a single observational signature that determines the evolutionary stage of such young objects, taken together, the observational properties listed above provide strong tools to distinguish the evolutionary status of IRAS 4C compared to IRAS 4A or IRAS 4B.

2. Observations and data reduction

2.1. JCMT

Spectral maps of the NGC 1333 IRAS 4 region were taken as a part of the JCMT Spectral Legacy Survey (SLS; Plume et al. 2007) with the 16–element Heterodyne Array Receiver Programme B (HARP–B) and the Auto–Correlation Spectral Imaging System (ACSIS) at the James Clerk Maxwell Telescope (JCMT[1]) on Mauna Kea, Hawaii. HARP–B consists of 16 pixels providing high-resolution (1 MHz, ∼ 1 km s^{-1}) maps of a 2′×2′ field. The original frequency coverage of 330–360 GHz of the survey was complemented by HARP maps at the window of the higher frequencies (360–373 GHz) as a result of additional proposals between 2007 and 2010. The observations were performed in a jiggle position switch mode to create maps of a 2′×2′ area with pixels spaced by 7.5″. Our maps were centered at RA = 03:29:11.3, Dec = 31:13:19.5 (J2000). The spectra were taken using an off–position at RA = 03:30:21.0, Dec = 31:13:19.5 (J2000) which is about 15′ east of the field center. The angular resolution of the JCMT is ∼ 15″ at 345 GHz which is equivalent to ∼ 3000 AU at the distance of NGC 1333 IRAS 4 (Choi et al. 2004). The beam efficiency is 0.63 (Buckle et al. 2009).

The raw time series files were reduced semi–manually using standard procedures from the Starlink software package [2] in combination with the ORAC Data Reduction pipeline (ORAC-DR). Each scan file was inspected and corrected for bad receptors, baseline subtraction and spike removal, before converting time series frequencies to 3–D data cubes. The pipeline output was further checked and corrected for remaining baseline issues, high rms noise level cubes or position issues using specific tasks from Starlink. The overall noisy band edges were ignored, allowing ∼ 0.85 GHz of bandwidth per frequency block to be used. The overall rms noise level is ranging between 0.005 and 0.05 K for the majority of the cubes with detected lines.

2.2. CARMA

In order to study the small–scale structure of IRAS 4C (RA = 03:29:13.64, Dec = 31:13:57.5 (J2000)), including dust prop-

[1] The James Clerk Maxwell Telescope has historically been operated by the Joint Astronomy Centre on behalf of the Science and Technology Facilities Council of the United Kingdom, the National Research Council of Canada and the Netherlands Organisation for Scientific Research.

[2] See http://starlink.eao.hawaii.edu/starlink

erties, we obtained single pointing interferometric CARMA [3] observations at 1.3 mm, between April and July 2014. The 15–element array excluding eight of 3.5-meter antennas consists of nine 6.1–meter diameter telescopes and six 10.4–meter diameter telescopes with a primary beam at 230 GHz of 47″and 28″ respectively.

In addition to the dust continuum emission, we observed the following molecular transitions: CO 2-1 (230.5 GHz), ^{13}CO 2-1 (220.4 GHz), C^{18}O 2-1 (219.6 GHz) and N_2D^+ (231.3 GHz), which are tracers of an envelope and/or outflow. These observations were performed in a dual polarization mode that provided us with a better sensitivity in D configuration. For the CO isotope lines, a 31 MHz bandwidth was used with 3–bit sample mode, which provides a good velocity resolution (∼ 0.13 km s^{-1}) and coverage (∼ 40 km s^{-1}), in order to trace the kinematics of the envelope as well as the outflow. These 4 molecular lines were observed simultaneously using 3 bands and the additional fourth band was set to the wide 500 MHz bandwidth for the continuum emission and calibration. The CARMA data are characterized by 2″ angular resolution (∼500 AU at the target distance) and ∼15 mJy/beam sensitivity. Because the typical dense cores and envelope sizes are around 5000 AU (Crapsi et al. 2005b), our data resolve the structures well.

We reduced and edited the visibility data using the MIRIAD software package (Sault et al. 1995).

3. Observational results

3.1. Single dish line detections and morphology

The JCMT data provide us with information about the spatial and velocity distributions of many different molecules. The majority of lines show clear emission towards the Class 0 IRAS 4A and IRAS 4B sources whereas fewer molecules show compact emission towards IRAS 4C (Figure 1).

Figure 2 shows the H_2CO $5_{1,5}$–$4_{1,4}$ emission as a representative example of the spatial distribution seen in all 3 sources. Emission from IRAS 4A and IRAS 4B and their surroundings is prominent with the strongest emission towards IRAS 4B. There is also significant emission towards the north of IRAS 4A**,** as a result of its strong outflow activity. The peak of the red wing emission (from +10 to +17 km s^{-1}) of H_2CO is also at that position. Weak emission of H_2CO can be seen also towards IRAS 4C, which is more compact. The red and blue wings trace the red–shifted and blue–shifted outflow activity from both IRAS 4A and IRAS 4B but there is no such signature from IRAS 4C at those velocities. In the same plot a fourth source of emission is also revealed towards the southwest of IRAS 4A, which we call IRAS 4–SWC (southwest clump) in this work.

The detected species (Table A.1–A.3) are divided into two groups. One group is characterized by narrow line profiles (FWHM ∼ 1–5 km s^{-1}) and compact spatial distribution (∼15–20″) and is therefore suggested to arise in the quiescent envelope (e.g. C^{17}O, HCO^+, H_2CS and N_2H^+). The other group is characterized by broad line profiles (FWHM ∼ 8–16 km s^{-1}) and extended emission (∼40″– 1′) and is therefore suggested to trace dynamical processes such as outflows (e.g. CO, HCN, CH_3OH and H_2CO).

Figure 3 shows the C^{17}O integrated intensity map (from +5 to +9 km s^{-1}) tracing the quiescent gas overplotted with the red (from +10 to +25 km s^{-1}) and blue (from -10 to +4 km s^{-1}) wings of the HCN 4-3 line profiles tracing the activity shifted from the LSR velocity (the signature of an outflow).

[3] Combined Array for Research in Millimeter-wave Astronomy; See https://www.mmarray.org

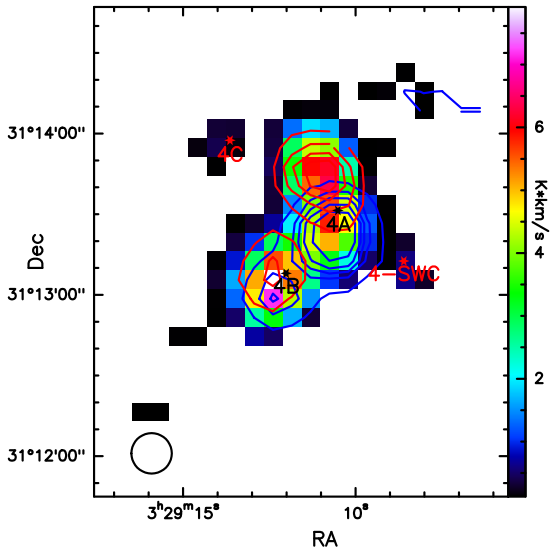

Fig. 2. Integrated intensity map (core; from +5 to +10 km s^{-1}) of H_2CO $5_{1,5}$–$4_{1,4}$ in colors, overplotted with its blue (from -5 to +5 km s^{-1}) and red (from +10 to +17 km s^{-1}) wing emission in blue and red contours respectively. H_2CO peaks towards IRAS 4B and shows a weak emission towards IRAS 4C but not connected to outflows. Note also the small peak to the southwest of IRAS 4A. The red and blue contour levels are set to 10, 30, 50, 70, 100 ×rms (rms: 0.02 K).

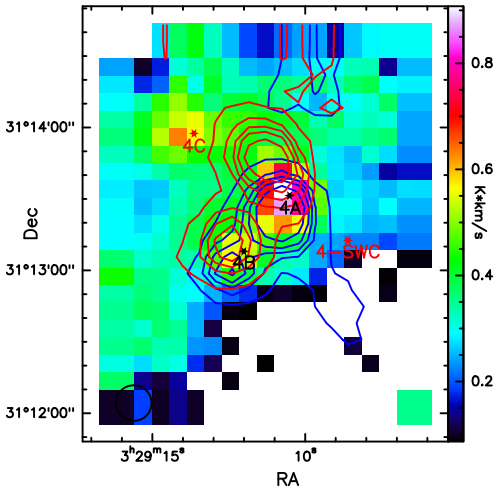

Fig. 3. Integrated intensity map (core; from +5 to +9 km s^{-1}) of C^{17}O 3–2 in colors, overplotted with the HCN 4–3 contours tracing outflow activity, namely red wing (from +10 to +25 km s^{-1}) in red contours and blue wing (from -10 to +4 km s^{-1}) emission in blue contours. The plot shows the presence of the bipolar outflows driven by IRAS 4A and IRAS 4B Class 0 objects. We do not see such activity towards IRAS 4C. C^{17}O is stronger towards IRAS 4C than towards IRAS 4B. The red and blue contour levels are set to 10, 30, 50, 70 and 100 ×rms (rms: 0.02 K). The contours on the top are due to more noisy map towards the edges.

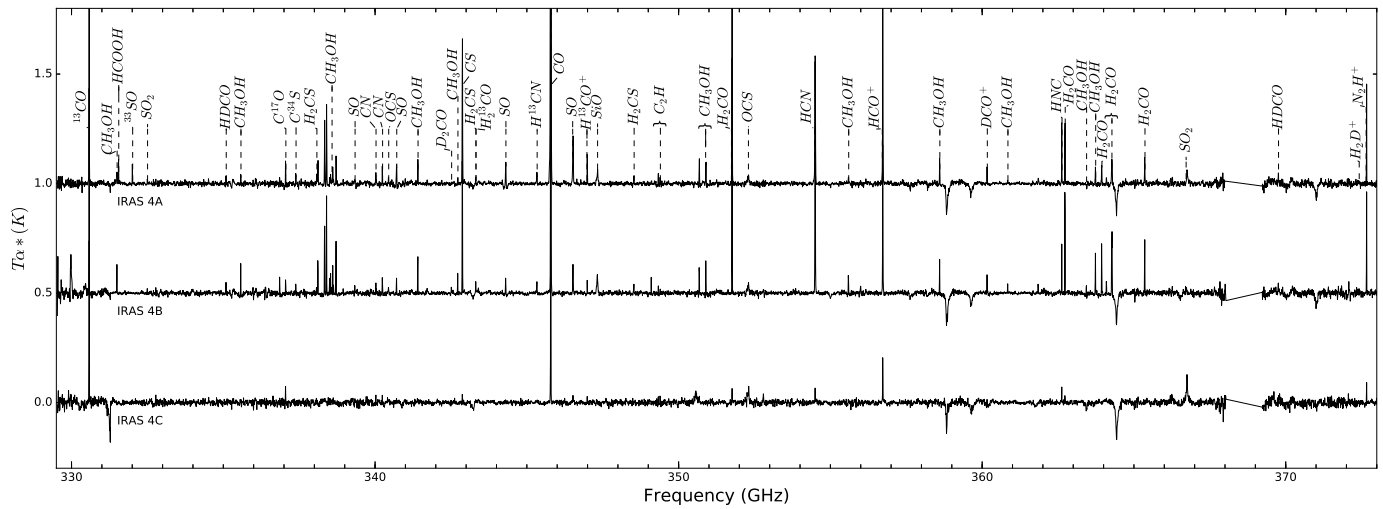

Fig. 1. Main line detections of the spectra extracted for the 3 positions of NGC 1333: IRAS 4A, IRAS 4B and IRAS 4C covering the full JCMT range 330–373 GHz. The gap seen at 368–369.5 GHz is due to poor atmospheric transmission. The spectra are plotted with a vertical offset at 0.3, 0.7 and 1.1 intensity levels (K) for easier comparison. The coordinates of the three sources IRAS 4A (RA = 03:29:10.51, Dec = 31:13:31.4 (J2000)), IRAS 4B (RA = 03:29:12.01, Dec = 31:13:08.0 (J2000)) and IRAS 4C (RA = 03:29:13.64, Dec = 31:13:57.5 (J2000)) are taken from Sandell & Knee (2001).

The IRAS 4A and IRAS 4B Class 0 objects both drive bipolar outflows first detected in CO and CS by Blake et al. (1995) and a few years later in millimeter transitions of SiO by Lefloch et al. (1998). The strong bipolar collimated outflow driven by IRAS 4A can also be seen in Figure 4, where IRAS 4B shows a compact outflow and IRAS 4C does not show a bipolar outflow, but a cone–like structure to the east of IRAS 4C. The continuum emission and the starting point of the cone show an east offset of 14″, and given the fact that IRAS 4C is the closest source it might be associated with it, but this is not clear from our observations. A water maser was reported by single–dish observations near IRAS 4C by Haschick et al. (1980), a fact that could indicate the presence of an outflow. However, several following interferometric surveys did not detect associated maser emission at the reported position (Rodríguez et al. 2002; Furuya et al. 2003; Park & Choi 2007). Figure 1 presented by Park & Choi (2007), shows that the previously reported H_2O maser is ∼25″to the north of IRAS 4A and west of IRAS 4C and follows the distribution of the well known outflow activity from IRAS 4A. This is an indication that this maser is not really connected to IRAS 4C.

Our CO maps are very similar to the ones presented by Yıldız et al. (2012), where the 6–5 transition is also included. IRAS 4A is a binary system (Looney et al. 2000) with a separation of 1.8″ (420 AU at a distance of 235 pc) and it is characterized by two outflows with different directions. The strongest outflow seen in CO is in the NE–SW direction, while other tracers such as H_2CO (Figure 2) show a more compact emission on the N–S axis. Similar findings are presented by Santangelo et al. (2015). The binary nature of IRAS 4A could explain these two different outflow morphologies observed in different tracers.

Figure 5 shows the SiO integrated intensity map in the full range from −11 to +23 km s^{-1}. The peak of this emission is northeast of IRAS 4A, following the red–shifted outflow activity from IRAS 4A as traced with methanol (CH_3OH, Figure 5). The spatial distribution of SiO follows the same pattern as the spatial distribution of the extracted outflow activity from CH_3OH. SiO traces even more energetic processes such as shocks (Duarte-Cabral et al. 2014). In these tracers IRAS 4C is absent, which may be an indication of less energetic outflow activity.

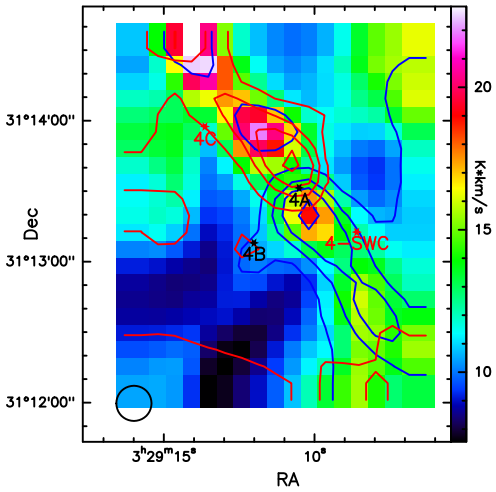

Fig. 4. Integrated intensity map (core; from +5 to +9 km s^{-1}) of CO 3-2 in colors, overplotted with the red wing (from +10 to +25 km s^{-1}) emission (red contours) and blue wing (from -10 to +4 km s^{-1}) emission in blue contours. The plot clearly shows the strong bipolar outflow driven by IRAS 4A Class 0 object. The red and blue contours levels are set to 100, 300, 500 and 800 ×rms (rms: 0.02 K).

N_2H^+ traces very well the distribution of the protostellar envelope and the gas surrounding the protostars, without emission from the IRAS 4–SWC source (Figure 6). The same figure shows that H_2D^+ is anti–correlated with the protostar positions, showing emission parallel to the IRAS 4A–4B direction. This covers a part of the area where the DCO^+ emission is extended. Deuterated species have been found to trace the coldest regions of gas, especially H_2D^+ whose main destroyer (CO) is frozen out in the grains (Crapsi et al. 2005b; Caselli et al. 1999). The distribution of H_2D^+ points towards a colder layer of gas that could explain the enhanced deuterated species.

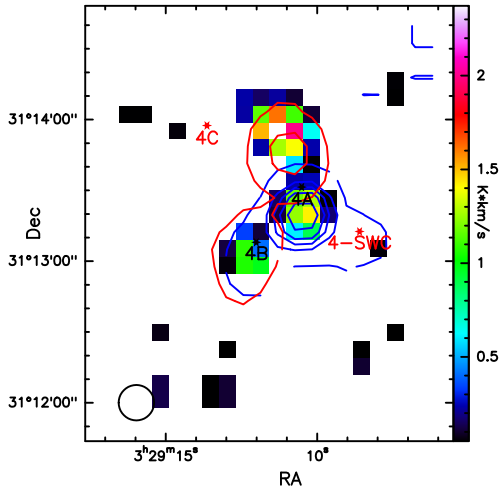

Fig. 5. Integrated intensity map (from -11 to +23 km s^{-1}) of SiO 8–7 in colors, overplotted with the blue (from -5 to +5 km s^{-1}) and red (from +9 to +15 km s^{-1}) wing emission from CH_3OH $7_{-1,7}$–$6_{-1,6}$ in blue and red contours respectively. The SiO peaks north of IRAS 4A close to the peak redshifted emission of CH_3OH and traces the shock activity in the region. No emission connected to IRAS 4C is observed. The red and blue contour levels are set to 5 30 50 70 100 and 150×rms (rms: 0.02 K).

The species that were detected in all 3 sources include HCN, HNC, HCO^+, $H^{13}CO^+$, DCO^+, N_2H^+, CO, ^{13}CO, $C^{17}O$, H_2CO C_2H, CN and CS. IRAS 4C shows significantly fewer transitions of these species, which are weaker by factors of 2 to 5 compared to IRAS 4A and IRAS 4B (Figure 1). The absorption features at 331.2, 358.8, 359.7, 358.9 and 359.6 GHz cannot be identified. They are very broad (FWHM ~75 km s^{-1}), and they are found at the edges of some datacubes, which likely makes them artifacts.

CH_3OH lines with upper energy levels E_{up}>35 K are missing from the spectrum of IRAS 4C, while the spectrum of IRAS 4A and IRAS 4B show CH_3OH lines with E_{up} up to 250 K. This trend is similar for the observed H_2CO lines towards the 3 sources. IRAS 4C does not show any associated SiO emission. H_2D^+ does not really peak toward any of the sources, but its spatial distribution reveals that it covers the space between them (Figure 6). A weak emission of 0.08±0.03 K (<3 RMS) is observed towards IRAS 4C but not towards the other sources. Some isotopologues such as $H^{13}CN$, $H_2{}^{13}CO$, $C^{34}S$, and deuterated species such as D_2CO and HDCO are also not detected in the spectrum of IRAS 4C (see §2 for noise levels), while they are present in the spectrum of IRAS 4A and IRAS 4B.

The new source, IRAS 4–SWC, is present in multiple observations including our maps of CH_3OH and H_2CO for E_{up}<60 K (RA = 03:29:08.6, Dec = 31:13:12.6 (J2000)). We aim to clarify the nature of the IRAS 4–SWC emission. If it is result of a separate dense core (prestellar or protostellar) we would expect a compact detection in continuum observations. Prestellar cores are typically detected in (sub–)millimeter dust continuum emission, in absorption at mid– and far–infrared wavelengths (Bacmann et al. 2000) and often show evidence of infall motions (Gregersen & Evans 2000). A protostar on the other hand, is associated with compact radio/centimeter continuum source accompanied with molecular outflows (i.e. CO), and/or evidence of an internal heating source (e.g. near/mid infrared emission). IRAS 4–SWC is not seen in mid and far–infrared wavelengths as compact emission (e.g. SCUBA, Spitzer; Sandell & Knee 2001) nor in absorption. Dense cores of 0.3$M_\odot$ at similar distances in Perseus are found to show a peak flux density of ~100 mJy/beam at 1.1 mm (σ~15 mJy/beam) after adopting a temperature of 15 K which is the value we determined for IRAS 4–SWC (Enoch et al. 2008). Given the lack of the predicted emission we conclude that IRAS 4–SWC is not a separate dense core. The fact that IRAS 4–SWC is mainly present only in outflow tracers (e.g. CH_3OH, SO) suggests that it could be an internal shock at a position of enhanced density in the IRAS 4A outflow.

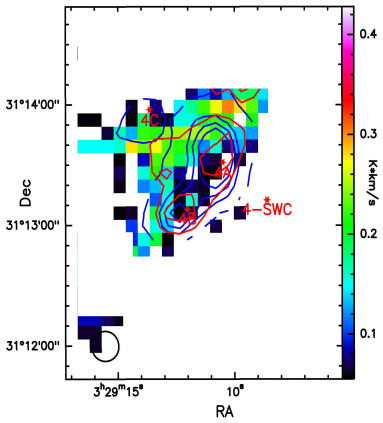

Fig. 6. Integrated intensity map (from +5 to +9 km s^{-1}) of H_2D^+ $1_{1,0}$–$1_{1,1}$ in colors, overplotted with N_2H^+ 4–3 in blue contours and DCO^+ 5–4 in red contours. The blue contours are set to 5, 20, 30, 40 ×rms (rms: 0.02 K) and the red contours are set to 3, 5 and 8×rms (rms: 0.03 K).

3.2. Line profiles

Figures 7, 8, 9 show representative examples of the observed line profiles towards IRAS 4A, IRAS 4B and IRAS 4C. In most cases, IRAS 4C shows narrow lines that can be fitted with a single Gaussian (<2 km s^{-1}) and are 2 to 5 times weaker than the other two sources (Table A.1–A.3). There are only few exceptions, e.g. $C^{17}O$, which is 2 times stronger towards IRAS 4C than IRAS 4B and has about the same intensity as towards IRAS 4A. Shah & Wootten (2001) also reported narrow lines towards IRAS 4C (NH_3; 1.4 km s^{-1}).

The majority of the lines towards IRAS 4A and IRAS 4B, can be fitted by two Gaussian components, a narrow (1–3 km s^{-1}) and a broad (5–12 km s^{-1}) with the broadest towards IRAS 4A tracing outflow activity. We observe 5 to 10 times broader lines in IRAS 4A and IRAS 4B compared to IRAS 4C. The fact that the line profiles from IRAS 4C do not show any signature of a broader outflow component (e.g. Figure 7) argues against an outflow along the line of sight. In the alternative case of an outflow in the plane of the sky, one would expect to observe lobes related to the outflow in the CO maps, which is not the case (Section 3.1). The cone-like structure observed in Figure 4 to the east of IRAS 4C could be a single lobe of an outflow from IRAS 4C, which is the nearest source. If IRAS 4C is at the same distance as IRAS 4A, it is possible that the stronger, more powerful outflow from IRAS 4A would drag the west outflow lobe from IRAS 4C with it, resulting in mixing of the two outflows. This scenario would explain the missing outflow signatures in

the line profiles of IRAS 4C for the extreme case that its outflow is located exactly in the plane of the sky, but the fact that the cone does not have its origin exactly in the continuum emission remains puzzling.

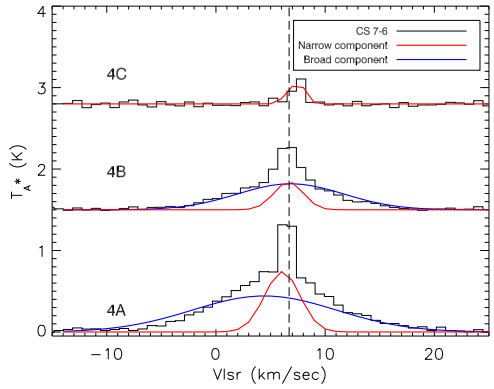

Fig. 7. Gaussian fit of a broad and a narrow component of CS 7–6 towards IRAS 4A, IRAS 4B and IRAS 4C sources (bottom to top). Dense gas tracers such as CS 7–6 do not show absorption but do show differences in line widths and strengths between the Class 0 objects IRAS 4A, IRAS 4B and the IRAS 4C source (single component).

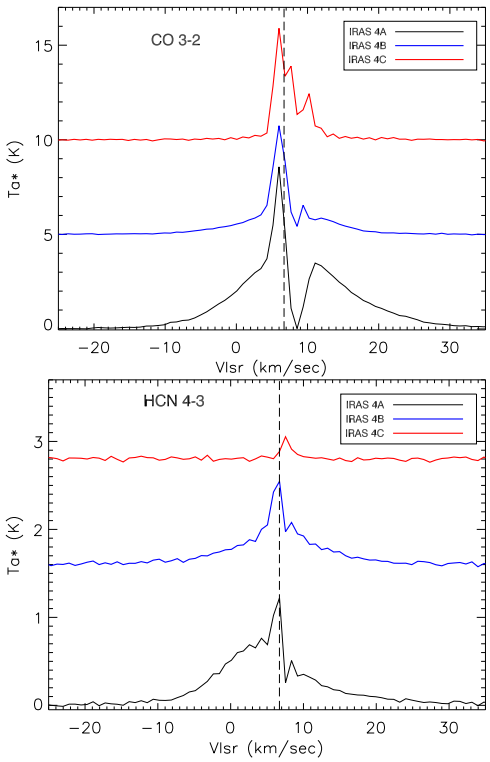

Fig. 8. CO and HCN line profiles for IRAS 4A, IRAS 4B and IRAS 4C sources (bottom to top). Note the absorption towards all positions. IRAS 4A shows a broad wing component, followed by IRAS 4B but IRAS 4C shows a steep line profile and only a very narrow red wing in both CO and HCN. The heavy absorption towards IRAS 4C makes it difficult to fit accurate Gaussians. The vertical line at +6.7 km/sec indicates the ambient velocity of IRAS 4A and 4B.

The absence of outflow signatures towards IRAS 4C could be a result of its evolutionary status. Broad velocity flows weaken as the core evolves (i.e. from Class 0 to Class I; Arce et al. 2007), which results in less clear spectral line evidence of the flows. In particular the outflow momentum reduces from $\sim 10^{-2}$ $M_\odot$ km s^{-1} to $\sim 10^{-3}$ $M_\odot$ km s^{-1}, as we move to more evolved stages (Machida & Hosokawa 2013). Outflows are also weaker in very early stages, in particular in the transition from a prestellar core to a Class 0 protostar, resulting in also less broad lines, owing to the lower masses involved in turbulence and/or infall. Thus the absence of outflow signatures towards IRAS 4C could mean either an earlier or a later evolutionary stage of the source compared to IRAS 4A and IRAS 4B. Orientation effects and/or mass may also play a crucial role in the observed differences.

Figure 8 presents the line profiles of HCN and CO. HCN shows an absorption feature towards IRAS 4A and IRAS 4B but not towards IRAS 4C while CO shows absorption features in all sources. We observe a velocity offset of ∼1 km s^{-1} between the peak intensities of IRAS 4A and IRAS 4B (+6.7 km s^{-1}) and IRAS 4C (+8 km s^{-1}). The absorption features can be interpreted as infall motions towards IRAS 4A and IRAS 4B which appear as inverse P–cygni profiles. In that case IRAS 4C does not show infall. Another possible explanation for the observed absorption is that there is a foreground gas and IRAS 4C is part of this foreground. The fact that the absorption of both sources appears at similar velocity with the peak intensities of IRAS 4C though, favors the foreground scenario.

Figure 9 shows examples of H_2CO and CH_3OH line profiles towards the 3 sources. Striking is the 1.5 to 2.5 times weaker emission of H_2CO and CH_3OH transitions toward the IRAS 4C source in comparison with the other 2 sources. We do not detect H_2CO transitions with E_{up}>65 K towards IRAS 4C. Regarding methanol (CH_3OH) lines, IRAS 4B shows the strongest emission among the sources for all observed transitions, while IRAS 4A shows about 2 times weaker emission but 1.5 to 2 times broader lines compared to IRAS 4B. IRAS 4C shows only CH_3OH transitions with E_{up}<35 K. The methanol lines toward IRAS 4B show a red wing ∼7 km s^{-1} at lower energies (E_{up}<100 K) indicative of an outflow activity and mostly a single component at higher energies (100 K <E_{up} < 200 K), which possibly arises in the dense quiescent parts of the protostellar envelope. The red wing at lower energies and the absence of blue component could be a result of absorption due to a dense, expanding, inner envelope. The methanol lines appear stronger in peak intensity towards IRAS 4B indicating a higher abundance, while in IRAS 4A the wings are broader and show a blue shifted wing indicating faster/stronger outflows. The formaldehyde lines follow the same pattern (Figure 9).

C_2H is one of the few species that show the strongest emission toward IRAS 4C (Figure 10). This species is thought to trace early stages of massive star formation (Beuther et al. 2008). However, Sakai et al. (2010) report very bright C_2H towards the low mass late Class 0 source L 1527. More likely the presence or absence of a particular species may signify some different chemistry rather than the final mass of a protostar, while for individual lines, excitation effects may play a role.

3.3. Velocity structure

The velocity distribution maps of several species (e.g. SO; Figure 11) show clearly that although the peaks for IRAS 4A and IRAS 4B appear at similar velocity (+6.7 km s^{-1}), IRAS 4C

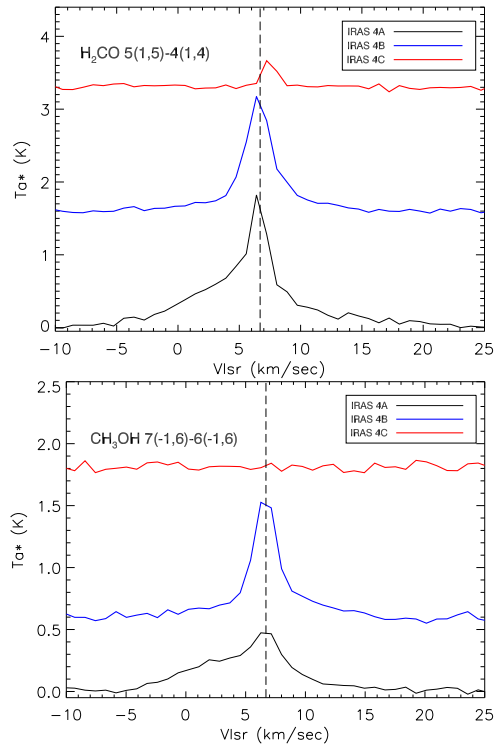

Fig. 9. Profiles of formaldehyde (top) and methanol (bottom) lines as observed towards the 3 sources IRAS 4A, IRAS 4B and IRAS 4C. IRAS 4C is present at the lower transitions where IRAS 4A is the strongest peak. At higher transitions IRAS 4B is the strongest peak. In all cases IRAS 4A shows the broadest profile among the 3 sources.

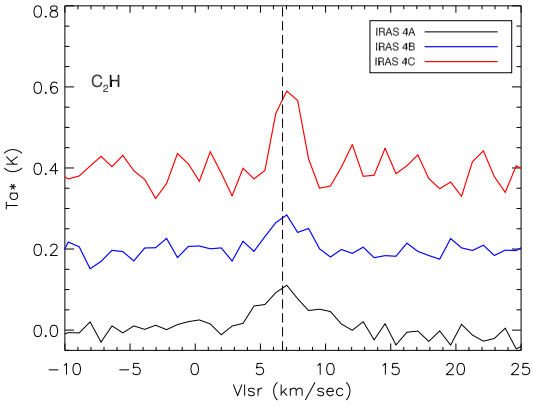

Fig. 10. Line profiles of C_2H (N=4-3, J=9/2-7/2, F= 4-3) towards IRAS 4A, IRAS 4B and IRAS 4C (bottom to top). C_2H is stronger towards IRAS 4C. The intensity of the other 2 lines are comparable, but IRAS 4A shows broader profile. The vertical line represents the ambient velocity of IRAS 4A and 4B at +6.7 km s^{-1}.

and its surrounding area peak at about 1 km s^{-1} higher velocity (+7.9 km s^{-1}).

IRAS 4–SWC peaks at about 1 km s^{-1} lower velocity (+5.6 km s^{-1}) which indicates an overall velocity gradient in the NE–SW direction (ΔV ~2.5 km s^{-1}), probably due to the structure of the ambient cloud. NGC 1333 is characterized mostly by

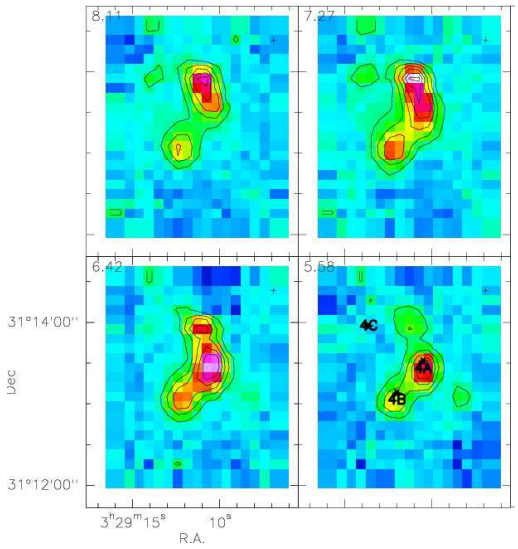

Fig. 11. Channel maps of SO 9(8)–8(7) obtained with JCMT, with the central velocities given in km s^{-1}. The emission from IRAS 4C appears at higher velocity channels (from +7 to +8 km s^{-1}) while IRAS 4–SWC at lower velocity channel (+5.6 km s^{-1}). The peak north to IRAS 4A at about +7 km s^{-1} can be associated with a outflow/shock from IRAS 4A.

the +8 km s^{-1} velocity component and it has been suggested that the IRAS 4 core (+6.7 km s^{-1}), is actually a smaller embedded cloud with a different velocity (Choi et al. 2004; Langer et al. 1996). The observed HCN absorption towards IRAS 4A and IRAS 4B at +7.84 km s^{-1} (Figure 8) is at a very similar velocity as the peak velocity (~8 km s^{-1}) of almost all the observed lines towards IRAS 4C (Table A.3). This coincidence could indicate that IRAS 4C might not be a member of the IRAS 4 cloud, but in the foreground. Although the observed differences may lead to question the membership of IRAS 4C in the IRAS 4 cloud, they are small enough to conclude that IRAS 4C is not at a significantly different distance compared to the other two objects.

3.4. Interferometric continuum and line emission

Our CARMA continuum observations at 1.3 mm reveal the dust emission from IRAS 4C which appears to trace a compact region (Figure 12). A 2d Gaussian fit of this emission gives a deconvolved component size of FWHM 1.79″× 1.35 ″(420×320 AU). The observed peak flux density of the continuum observations is 51 mJy/beam with a rms of ~ 3mJy. Tobin et al. (2015) had about 3 times higher resolution resulting in consequently a smaller deconvolved size of FWHM 0.51″× 0.22 ″(120×52 AU). Di Francesco et al. (2001) using IRAM PdBI (Beam FWHM: 2″× 1.7 ″) towards IRAS 4A and IRAS 4B report a deconvolved size of 920×720 AU and 600×560 AU respectively. The reported differences are a result of the different angular resolutions among the studies.

The 2–1 transitions of CO, ^{13}CO and C^{18}O have also been detected in our CARMA data. The integrated intensity peaks of the blue (from +5 to +6.5 km s^{-1}) and red (from +8.5 to +11 km s^{-1}) wing of ^{13}CO show a small offset (<1″) compared to the peak intensity of the continuum (Figure 12), with the blue to be in similar direction with the outflow as indicated by Spitzer observations (further discussion in Sec. 4.1). The CO and ^{13}CO lines show strong absorption at source velocities

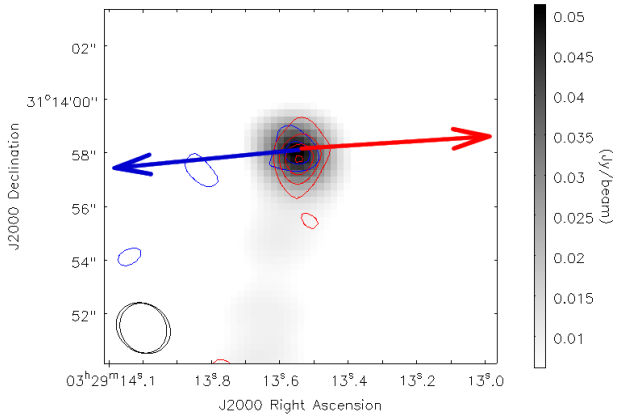

Fig. 12. CARMA continuum observations of NGC 1333/IRAS 4C at 1.3 mm (grey–scale) overplotted with the red and blue wings of ^{13}CO 2–1. The velocity range of the line is between +5 and +11 km s^{-1}, and a siginificant part of the emission has been resolved–out by the interferometer at the source velocity, while we still get emission from the wings. The peaks of the blue (from +5 to +6.5 km s^{-1}) and red (from +8.5 to +11 km s^{-1}) wing show a small offset compared to the peak intensity of the continuum. The blue contours levels are set to 0.04 0.06 0.08 0.10 and 0.13 Jy/beam (rms~0.014 Jy/beam) and the red at 0.06, 0.09, 0.12, 0.15, 0.18 Jy/beam (rms~0.02 Jy/beam). The ellipse shows the beam size and shape at this wavelength (2.12″×1.81″). The arrows represent the direction of blue–shifted and red–shifted outflow components (Tobin et al. 2015).

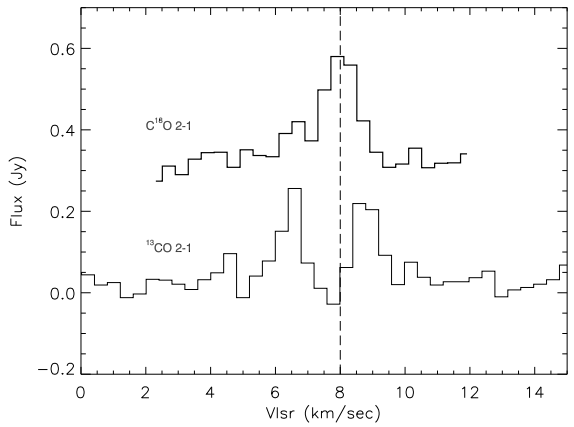

Fig. 13. CO isotopologues as observed with CARMA towards NGC 1333/IRAS 4C. ^{13}CO shows broader profile and significant part of the emission has been possibly resolved–out by the interferometer, while C^{18}O shows only narrow emission. The vertical line at +8 km s^{-1} is the velocity of the C^{18}O peak. The plotted flux offset between the lines has been chosen for easier comparison. ^{12}CO is not shown as it is heavily affected by absorption making its use very difficult.

(~+8 km s^{-1}) possibly as a result of resolved–out emission by the interferometer while C^{18}O shows only narrow emission with a FWHM of 1.7±0.2 km s^{-1} at +7.9±0.1 km s^{-1} (Figure 13). Similar velocity offsets are observed also with our JCMT data (e.g. Figure 7).

We obtain a ~7σ detection of N_2D^+ near IRAS 4C, which has been previously observed towards all 3 sources (single dish; Friesen et al. 2013). Our maps reveal an offset between the continuum source and the N_2D^+ emission of 8.5″, which corresponds to 1900 AU (Figure 14). An offset up to 2000 AU between N_2H^+ 1–0, that traces the envelopes of the protostars and the N_2D^+ 2–1, 3–2 has been previously reported by Tobin et al. (2013) towards 8 protostellar objects and by Lee et al. (2015) towards 3 protostars in Perseus. N_2D^+ is expected to arise from environments where CO is depleted. Our finding suggests that this happens in a region offset from the dense core.

4. Evolutionary constraints

In our attempt to distinguish the evolutionary status among the 3 sources we mainly study the properties of the outflows which are found to have speeds of 10–20 km s^{-1} (Arce & Sargent 2006) for Class 0 objects and maximum of 3 km s^{-1} for a FHSC (Machida et al. 2008; Tomida et al. 2010), the temperature among the sources which increases as a protostar evolves, and the deuterium fractionation which can be used as a chemical clock (Belloche et al. 2006; Fontani et al. 2011, 2014).

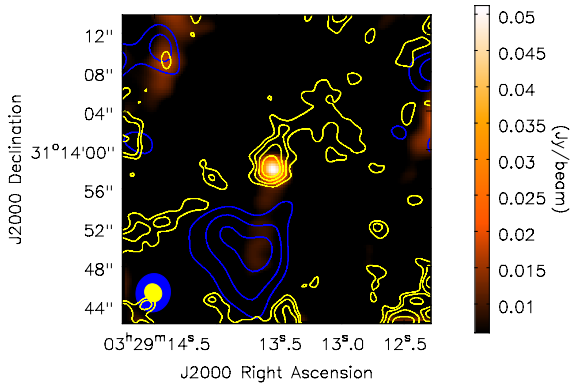

Fig. 14. Continuum emission towards IRAS 4C in colors, overplotted with the N_2D^+ 3–2 emission with blue contours at 0.45, 0.6, 0.7, 0.8 and 0.95 Jy/beam (rms~15 mJy/beam) and with the C^{18}O 2–1 emission with yellow contours at 0.04, 0.08, 0.10, 0.14, 0.20 and 0.29 Jy/beam (rms~14 mJy/beam). We observe an offset between the continuum source and the N_2D^+ of 8.5″. The beam sizes of the continuum (yellow) and the lines (blue) are also plotted with in the bottom left corner.

4.1. Properties of the outflows

We have mapped the NGC 1333 IRAS 4 region in CO 3–2 (JCMT; Figure 4). The spectra show deeply self–absorbed line towards all the 3 sources, broad wings towards IRAS 4A (FWHM~22.0±2 km s^{-1}) and IRAS 4B (FWHM~15.0±1 km s^{-1}) and a weak red wing signature from IRAS 4C (FWHM~5.0±0.4 km s^{-1}). The accurate fitting with Gaussians is difficult due to the heavy absorption, especially towards IRAS 4C which shows a much narrower line profile (Figure 8). Our ^{13}CO 3–2 JCMT line profiles though, can be fitted well with a single narrow com-

ponent of FWHM~1.9±0.1 km s^{-1} towards IRAS 4C, while IRAS 4A can be fitted with a 2–component Gaussian, a narrow one of FWHM~2.0±0.1 km s^{-1} and a broad one of FWHM~10.0±2 km s^{-1}. The line profile of IRAS 4B can also be fitted with only a single component of FWHM~2.4±0.1 km s^{-1}.

To search for compact outflows which single-dish observations may not pick up, high–resolution interferometric CO or H_2O observations toward protostellar cores are required (CARMA; Figure 12).

^{13}CO (J = 2-1) traces the low–velocity outflow in most class 0 protostars (Arce & Sargent 2006) but has been observed also in the inner envelope and the disk of extremely young protostars (e.g. L1527 IRS). To search for an outflow towards IRAS 4C, we use the ^{13}CO line and integrate the velocities of the emission excluding the lack of emission which is possibly due to the spatial filtering by interferometer from +6.5 km s^{-1} to +8.5 km s^{-1} (Figure 13). We get a narrow velocity range from +5 to +6.5 km s^{-1} for the blue shifted emission and from +8.5 to +11 km s^{-1} for the red shifted emission and we observe a small offset compared to the dust continuum emission, indicating a potential low–velocity outflow (Figure 12). We find an offset to the blue and red component of ^{13}CO that corresponds to a P.A. of ~29° while Tobin et al. (2015) found a P.A. of ~-21° for C^{18}O 2–1 using the B and C–array CARMA configuration. In that work, this offset is interpreted as a potential rotation signature, but due to poor S/N a Keplerian rotation could not be tested. A VLA 8–mm image of IRAS 4C at ~0.08″ resolution shows also a dust emission connected to a disk–structure and not outflow (Segura–Cox et al. 2015, submitted). Spitzer data have revealed nebulosity showing a scattered light cone which has an origin at the location of the protostar (e.g. Fig. 19; Tobin et al. 2015). Thus the most likely direction of the outflow is orthogonal to the plane of the disk. This is not the direction that our ^{13}CO shows and we measure an offset ~50° between our ^{13}CO and the C^{18}O which indicates that the 2 isotopologues do not trace exactly the same gas.

We measure ΔV =1.5 km s^{-1} for the blue shifted emission and ΔV =2.5 km s^{-1} for the red shifted emission. Some amount of the wing emission might also have been resolved–out by the interferometer. Still the observed velocity range for the potential outflow is very narrow indicating at best a very slow outflow (~2 km s^{-1}).

The characteristic outflow velocity V_{obs} that we measure provides a lower limit which can be corrected to the real flow velocity V_{flow} if the inclination angle *i* is known, using

$$V_{\rm flow} = \frac{V_{\rm obs}}{\sin i} \quad (2)$$

Following the suggestion from Tobin et al. (2015) that IRAS 4C contains a disk nearly at edge-on inclination, which corresponds to an outflow inclination angle of < 10°, adopting an angle of 5° we derive velocities up to 17 km s^{-1} for the blue shifted emission and up to 28 km s^{-1} for the red shifted emission which are an order of magnitude higher than the measured ones. In this case, we can explain the narrow lines but we cannot explain why the outflow is not spatially visible in our larger JCMT maps (Figure 4). We cannot exclude the scenario that our ^{13}CO emission is actually tracing the disk and not the outflow as suggested by Tobin et al. (2015).

At the same time IRAS 4B shows a compact outflow with an inclination close to 90° (Maret et al. 2009), which means that it is almost perpendicular to the plane of the sky and the observed velocity is the maximum it can have. The morphology of the IRAS 4A outflow indicates an inclination close to 20° which means that the observed velocities are underestimated by about a factor of 3. The inclination of both outflows have been calculated before using the masers associated with them, which provided proper motion and radial velocity measurements (Marvel et al. 2008). In that work both maser outflows were found to be nearly in the plane of the sky (2° for IRAS 4A, 13° for IRAS 4B) with the IRAS 4B estimate being more uncertain. Although in the studies mentioned above the inclination of IRAS 4B varies a lot, in each case IRAS 4A appears to drive the most powerful outflow close to the plane of sky and thus underestimated. The outflow velocities of IRAS 4A are at least 4 times larger than IRAS 4B which may indicate that IRAS 4A is a less evolved source than IRAS 4B. One must remember that 4A is a binary though. In particular, there is evidence that the source to the NW (A2) has masers while the source to the SE (A1) does not have masers (e.g. Park & Choi 2007). The H_2O masers require the existence of warm dense shocked gas (Elitzur et al. 1992), and mainly disks and outflows in YSOs fulfill these criteria. Thus A2 is probably more evolved than A1 source to the SE.

4.2. Mean envelope temperature

The determination of the temperature is another crucial parameter that we use to distinguish between the different evolutionary stages among objects with the same luminosity. We derive the kinetic temperature of IRAS 4 region using the H_2CO lines which have been found to be good tracers of kinetic temperatures. We use the most recent collisional rate coefficients as derived by Wiesenfeld & Faure (2013) and the Einstein coefficients from the JPL database (Pickett et al. 1998).

We used the non–LTE radiative transfer program RADEX (van der Tak et al. 2007) to compare the observed integrated intensity fluxes with a grid of models for deriving kinetic temperatures. For the model input we used the molecular data from the LAMDA database (Schöier et al. 2005). RADEX predicts line intensities of several molecular transitions for a given set of parameters: kinetic temperature, column density, H_2 density, background temperature, and line width.

We perform a χ^2 minimization to fit all the observed o–H_2CO and p–H_2CO fluxes simultaneously (up to 7 lines, Table A.1), using

$$\chi^2 = \sum_{i=1}^{n} \frac{(O_i - E_i)^2}{E_i} \quad (3)$$

integrated over the velocity range from +5 to +9 km s^{-1}, which corresponds to the narrow emission. In this way we try to limit the contribution of the outflows and perform the analysis under the assumption that we trace the same gas. The χ^2 (Eq. 3) was computed as the quadratic sum of the differences between the observed (O_i) and the synthetic (E_i) line intensities for a range of kinetic temperatures (7 K<T_{kin}<120 K), a column density of 2×10^{14} cm^{-2} and H_2 density of 3×10^5 cm^{-3}. These volume and column densities have been obtained from the analysis by Maret et al. (2004) towards IRAS 4A and IRAS 4B, which is based on data at similar angular resolution as ours (JCMT, IRAM; 9–17″ Maret et al. 2004). Adopting these values for the entire cloud suffers from uncertainties (see below) since it is expected that the rest of the cloud is most likely characterized by smaller densities. In addition, the temperature of the background radiation field (CMB) is set to 2.73 K and the line width to 1.8 km s^{-1} that approximates the value that we have measured

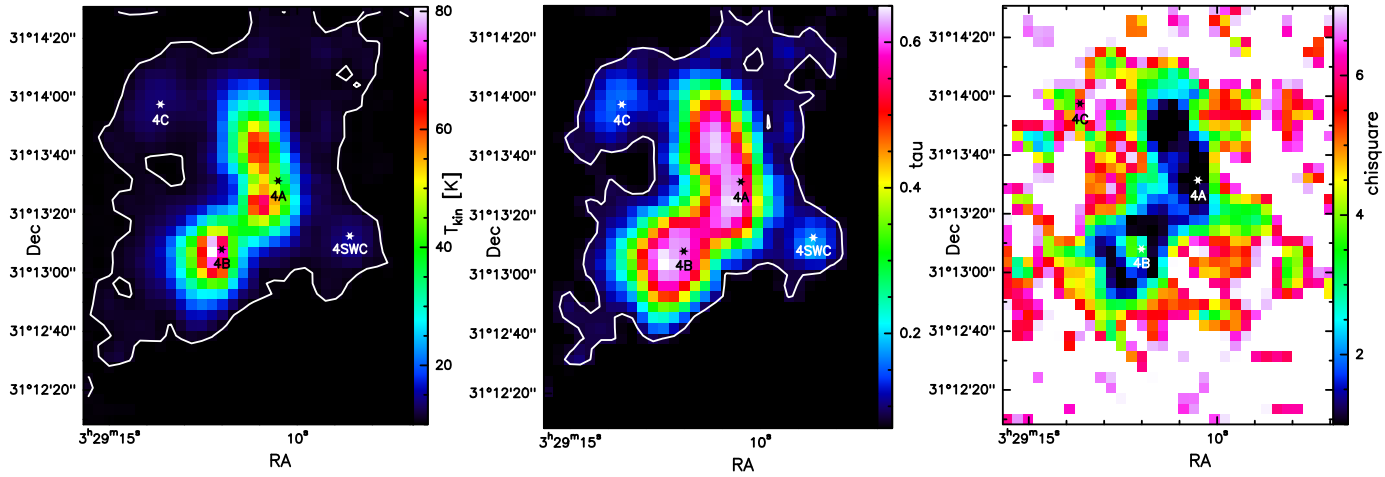

Fig. 15. Kinetic temperature map of NGC 1333 IRAS 4 (left). During the fitting procedure all the 7 H_2CO detected lines are taken into account for the positions with S/N >3. The white contour shows the region **where** at least 2 lines were detected with S/N >3. The kinetic temperature is higher towards the Class 0 objects IRAS 4A (~ 45 K) and IRAS 4B (~ 80 K) while it is significantly lower towards IRAS 4C (~ 12 K). Note also the compact emission towards IRAS 4–SWC (~ 15 K), which has been observed in channel maps of other molecules (e.g. CH_3OH, SO, Figure 11). The tau map of H_2CO $5_{0,5}$–$4_{0,4}$ presents values in the optically thin regime throughout the cloud (middle; ~0.1–0.7). The best resulting χ^2 vary between ~1–5 in the region of the sources (right).

throughout the cloud for the narrow component. Finally, in our calculations we assume a fixed ortho to para ratio of o–H_2CO/p-H_2CO = 3 and e-CH_3OH/a-CH_3OH of 1.

Figure 15 presents the kinetic temperatures of our modeling results, which vary between ~ 8 – 80 K with the highest value stemming from IRAS 4B. The map shows several local peaks with the global one towards IRAS 4B. Core IRAS 4A is not a temperature peak but rather the map shows two peaks northeast (~15″) and southeast (~5″) of IRAS 4A (~ 60 K). The gas that surrounds IRAS 4A and IRAS 4B is characterized by T_{kin} ~15–30 K. Two weaker local peaks are observed towards IRAS 4A and IRAS 4–SWC positions. Figure 15 presents the map of the H_2CO $5_{0,5}$–$4_{0,4}$ optical depth, which corresponds to the optically thin regime (~0.1–0.65) and the best fit χ^2 which is lowest (~1) towards IRAS 4A and the surrounding gas. Interestingly, the τ map peaks at the position of IRAS 4A, while T_{kin} map peaks at IRAS 4B. Only IRAS 4C shows up as a local peak in both the optical depth (i.e., column density) and kinetic temperature. The τ map shows also the two distinctive peaks towards IRAS 4A and IRAS 4B and its entire distribution follows the morphology of the kinetic temperature map.

Our kinetic temperature estimates towards the Class 0 objects IRAS 4A and IRAS 4B are 45 K and 80 K respectively while it is lower towards IRAS 4C (~ 12 K). Deutero–ammonia observations presented in Shah & Wootten (2001) point also towards very cold conditions towards IRAS 4C (15 K). IRAS 4–SWC is characterized by a kinetic temperature ~15 K and it can be a result of an internal shock connected to the outflow of IRAS 4A or a separate core, as discussed in Sec. 3.1.

Maret et al. (2004) had performed a H_2CO study towards a sample of 8 low mass protostars, including IRAS 4A and IRAS 4B. The collisional rate coefficients that were used in that study were taken from Green (1991). Our results are in excellent agreement with those Maret et al. (2004) reported (50 K for IRAS 4A; 80 K for IRAS 4B), especially given the different observations and collision rates used. In their analysis they used pointed observations towards IRAS 4A and IRAS 4B, thus no analysis was performed towards IRAS 4C and their H_2CO observations were taken from IRAM and JCMT, allowing them to measure more lines but at different angular resolutions.

To have a sense of the uncertainties in the above calculations, we have run additional models towards IRAS 4A and IRAS 4B, where the largest number of lines has been detected. For these models we varied the column density between 2×10^{12} cm^{-2} and 2×10^{16} cm^{-2}. We find a best fit column density of 5×10^{14} cm^{-2} for IRAS 4A and 3×10^{14} cm^{-2} for IRAS 4B which are 2.5 and 1.5 times higher than the previously adopted value of 2×10^{14} cm^{-2}, but the same order of magnitude. These values result in temperatures of 30 K for IRAS 4A and 64 K for IRAS 4B which are 1.5 and 1.2 times lower than the values we obtained above. IRAS 4B remains warmer than IRAS 4A while their absolute temperature difference remains to be ~35 K, making more prominent the temperature difference among the 2 systems.

Since we do not have a way to accurately measure the column density of IRAS 4C, and the other 2 sources were found to have higher column density than the adopted, we ran RADEX towards IRAS 4C for a higher N(H_2CO) adopting a value of 1.5 times higher that before, 3×10^{14} cm^{-2}. The increase in column density results in a kinetic temperature of ~8 K which is lower by 4 K compared to our previous estimation and maintains the IRAS 4C the colder among the sources. We also ran our calculations for 1.5 times lower column density using 7.5×10^{13} cm^{-2} a value that results a temperature of ~18 K which is 1.7 times higher than what we obtained in our analysis. Even in that case IRAS 4C remains to be the coldest among the sources with absolute differences of ~20 K and ~40 K with IRAS 4A and IRAS 4B respectively.

To test the assumption of constant volume density in our analysis, we have re–run our calculations for $n_{H_2} = 10^6$ cm^{-3} and 10^4 cm^{-3} for the entire cloud. The lower value of 10^4 cm^{-3} was adopted because the cloud around the compact objects is most likely characterized by smaller densities. In both cases the distribution of the kinetic temperature is the same as seen in Figure 15, but the values vary. For the higher density the temperature is characterized by significantly lower values (7 K<T_{kin}<22 K). Once more IRAS 4B is the warmest (~20 K), followed by

IRAS 4A (~16 K) and IRAS 4C (~8 K). For the lower density the cloud is characterized by temperatures 20 K<T_{kin}<82 K resulting ~ 60 K for IRAS 4B, ~ 35 K for IRAS 4A and ~ 16 K for IRAS 4C. This result indicates that our solution is more sensitive to higher densities leading to an overestimation of temperatures for IRAS 4A and IRAS 4C at the adopted n_{H_2} = 3×10^5 cm^{-3}, since they were found to be denser in our approach as described in Sec. 4.3. Although the absolute values for kinetic temperatures vary with the different assumptions, IRAS 4B remains the warmest and IRAS 4C the coldest among the 3 sources in all our calculations.

4.3. Mass and density

We use our CARMA continuum observations to estimate the gas mass (Equation 4) and the H_2 column (Equation 5) and volume density of IRAS 4C. We calculate these parameters via:

$$M_{gas} = \frac{S_\nu d^2 \alpha}{\kappa_\nu B_\nu(T_d)} \quad (4)$$

where S_ν = 0.061 Jy is the total flux density after fitting a 2D–Gaussian of 2.3″×2.1″, α = 100 is the gas to dust ratio, κ_ν(1.3 mm) = 0.89 cm^2 g^{-1} is the dust opacity per unit mass (Ossenkopf & Henning 1994) and $B_\nu(T_d)$ is the Planck function at dust temperature T_d (~12 K; H_2CO analysis described at 4.2). We find a M_{gas} = 0.16 $M_\odot$. We adopt a distance d of 235 pc. We calculate the column density using

$$N(H_2) = \frac{I_\nu \alpha}{2 m_H \Omega_b \kappa_\nu B_\nu(T_d)} \quad (5)$$

where I_ν is the peak flux density (0.048 Jy/beam), m_H is the mass of hydrogen and Ω_b is the beam solid angle. The resulting N(H_2) = 1.5×10^{24} cm^{-2} while the volume density assuming 2″ diameter for the adopted area as determined by a 2d Gaussian fit, is~3.1×10^8 cm^{-3}. This value is higher by 3 orders of magnitude compared to the values obtained by Maret et al. (2004) for IRAS 4A and IRAS 4B (3×10^5 cm^{-3}) and the one we have adopted for IRAS 4C for our H_2CO analysis (3×10^5 cm^{-3}; 4.2) under the assumption that the 3 sources are characterized by similar volume densities, but the scales are different since the CARMA beam is ~10× smaller and thus trace denser region.

Smith et al. (2000) derived masses of 10.9 $M_\odot$ for IRAS 4A, 6.9 $M_\odot$ for IRAS 4B and 2.9 $M_\odot$ for IRAS 4C using the SCUBA 850μm continuum map of NGC 1333/IRAS 4, with a FWHM of the beam ~16″ and assuming the same temperature (30 K) for the 3 sources. In that work they had considered the CO 3–2 line contamination in the 850 μm SCUBA passband, as a possible cause of an underestimation of the calculated spectral index and overestimation of the masses, but it could still not explain the low spectral indices observed towards the three sources.

The mass of IRAS 4C that we obtain is about an order of magnitude lower but the CARMA beam is ~10 times smaller. In addition we use the most recent distance estimate of 235 pc (Hirota et al. 2008), compared to their distance of 350 pc (Herbig & Jones 1983). Correcting for the distance and the temperature and using their reported values for total and peak flux density and their angular resolution we find a volume density of 6×10^6 cm^{-3}, which is about 2 orders of magnitude lower than the one obtained from the CARMA data, providing an evidence of a density gradient at IRAS 4C. We follow the same process for IRAS 4A and IRAS 4B using a FWHM ~25″ as a result of the Gaussian fit, and we measure the values of 2×10^6 cm^{-3} for IRAS 4A and 5×10^5 cm^{-3} for IRAS 4B. So we find that IRAS 4C is 3 times denser than IRAS 4A and IRAS 4A is 4 times denser than IRAS 4B. Since our CARMA observations do not cover IRAS 4A and IRAS 4B we cannot further investigate possible density gradients.

Lastly, for a direct comparison, we determine the masses of the sources in a resolution similar to our JCMT maps. For this purpose, we use the SCUBA data (Smith et al. 2000), adopting the more recent distance of 235 pc and the temperatures we derived in Sec. 4.2 and we calculate masses (Eq. 4) of 2 $M_\odot$ for IRAS 4A, 0.6 $M_\odot$ for IRAS 4B and 1.5 $M_\odot$ for IRAS 4C. This is the first time that IRAS 4C appears with a higher mass than IRAS 4B due to the fact that we do not use the same temperatures for all 3 sources, as previous studies, but the ones determined in Sec. 4.2. The derived masses and column densities are very sensitive to the adopted opacity and temperatures which can cause a difference up to a factor of 3–5 given the temperature uncertainties discussed above.

4.4. Depletion of CO

Carbon monoxide and its isotopologues are broadly used as a tracer of N(H_2) in studies of the interstellar medium. The most abundant ^{12}CO, can only provide a lower limit of the column density and the mass of the region since it is often optically thick in typical conditions of the molecular clouds. The less abundant isotopologues can then been used (e.g. ^{13}CO, C^{18}O), assuming optically thin emission.

To estimate the spatial distribution of N(CO), we use the C^{17}O 3-2 line, assuming a constant ^{16}O/^{17}O of 2000 (Wilson 1999). We run RADEX in order to derive the column density of C^{17}O, using the gas temperature map as determined from the H_2CO analysis and a constant volume density of 3×10^5 cm^{-3}. We derive N(CO) for the region where T_{peak}>3 rms, to be in the range of 2×10^{17} cm^{-2} – 9×10^{17} cm^{-2} (Figure 16).

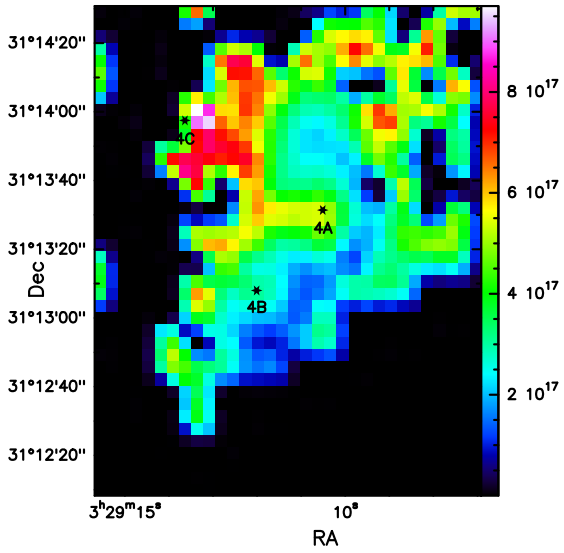

Fig. 16. Synthetic CO column density as determined fitting the peak intensities for the range from +5 to +9 km s^{-1}.

The higher value is close to IRAS 4C. This is a result of low kinetic temperature of IRAS 4C compared to the other two sources (~12 K) while the intensity of C^{17}O line is stronger to-

wards IRAS 4C than towards the warmest IRAS 4B (Figure 17). In order to be able to fit the relatively high intensity towards IRAS 4C, for so low kinetic temperature RADEX requires higher column density, given the fact that we use a constant volume density.

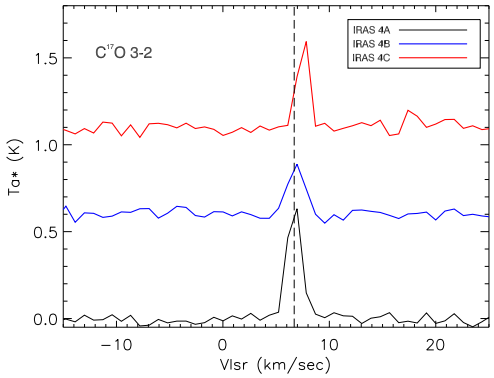

Fig. 17. $C^{17}O$ 3-2 line profiles towards IRAS 4A, IRAS 4B and IRAS 4C. The line is strongest towards IRAS 4A followed by IRAS 4C and then IRAS 4B.

In order to derive the N(CO)/N(H_2) for the 3 sources we use Equation 5 applying the peak flux densities reported by Smith et al. (2000) from the 850μm continuum. In this way we ensure that the angular resolution between continuum and CO observations is about the same (HPBW ~ 13.5 ″) and thus that we trace the same amount of gas. For the temperature we use 45 K, 80 K and 12 K for IRAS 4A, IRAS 4B and IRAS 4C respectively as have been determined in Sec. 4.2. We find the column density N(H_2) towards IRAS 4A, IRAS 4B and IRAS 4C to be 2.4×10^{23} cm^{-2}, 1.3×10^{23} cm^{-2} and 3.6×10^{23} cm^{-2} resulting N(CO)/N(H_2) of 2.4×10^{-6}, 3.8×10^{-6} and 1.2×10^{-6}. These values are ~ 1.5 – 2 orders of magnitude less than the canonical [CO]/[H_2] of 10^{-4} indicating significant depletion of CO.

The CO depletion factor, f_D can be calculated via:

$$f_D = \frac{X^E_{CO}}{X^O_{CO}} \quad (6)$$

where X^E_{CO} is the expected abundance of CO relative to H_2 (10^{-4}) and X^O_{CO} is the ratio between the observed N(CO) and the observed N(H_2).

We determine a f_D of 42, 26 and 83 for IRAS 4A, IRAS 4B and IRAS 4C respectively. The highest degree of CO depletion is observed towards the coldest of the sources, IRAS 4C, while the lowest degree of CO depletion towards the warmest source, IRAS 4B, as expected (e.g.; Bacmann et al. 2002). Our solution is dependent on the assumed parameters, including the resulting kinetic temperature for the 3 sources and the assumption that H_2CO and $C^{17}O$ trace the same gas. As discussed also in Sec. 4.2, IRAS 4C is the coldest of the sources under each assumption and thus although the absolute values of depletion factors may vary, the estimated trend between the sources will remain.

4.5. Deuteration

The deuterium fractionation (e.g. [N_2D^+]/[N_2H^+]) is another factor to estimate the evolutionary stage of IRAS 4C. More specifically, the [N_2D^+]/[N_2H^+] can be used as a chemical clock (Belloche et al. 2006; Pagani et al. 2013; Fontani et al. 2014) and has been measured to be ~ 15 – 20 % for prestellar cores (e.g. L1544) and ~ 5 – 10 % for Class 0 objects (e.g. L1521F). A measurement between these two limits is an indication for an object for which the evolutionary stage lies between these two early star formation stages. The cosmic ratio [D]/[H]=1.5×10^{-5} (Linsky et al. 1995) and that higher observed values are typical for low–mass dense cores (e.g.; Crapsi et al. 2005b; Parise et al. 2006). This can be explained due to the fact that at very low temperatures the reaction $H_3^+ + HD \Longleftrightarrow H_2D^+ + H_2 + \Delta E$ is driven strongly to the right increasing the abundance of H_2D^+, in combination with the undergoing freeze out of CO which decreases the H_2D^+ destruction rate (e.g. prestellar cores Bacmann et al. 2003). This process leads to enhancement of H_2D^+ and the D atom passes down to other species leading to formation of more deuterated species such as N_2D^+. We do not have N_2D^+ observations towards all the sources and our N_2H^+ emission is from JCMT data making the determination of [N_2D^+]/[N_2H^+] impossible for our dataset.

We used RADEX to model the observed emission in HCO^+, $H^{13}CO^+$ and DCO^+. The collision rates of HCO^+ and DCO^+ with H_2 were adopted from Flower (1999). The critical densities n_{cr} of HCO^+ 4–3 and DCO^+ 5–4 at 50 K are ~9.1×10^6 cm^{-3} and ~9.3×10^6 cm^{-3}, calculations based on Schöier et al. (2005).

For this purpose we used the kinetic temperature map resulting from the H_2CO analysis and a constant volume density of 3×10^5 cm^{-3} for the entire cloud. Fitting the integrated intensities of the lines for each spatial point enabled us to produce the column density maps of $H^{13}CO^+$, DCO^+. We find column densities between 8×10^{12}–4×10^{13}cm^{-2} for $H^{13}CO^+$ with the higher value close to IRAS 4C and 8×10^{13}–1.5×10^{14}cm^{-2} for DCO^+. HCO^+ is usually optically thick, something that we were able to test by determining the observed HCO^+ 4-3 / $H^{13}CO^+$ 4-3 ratio of the peak intensities for the range from +5 to +9 km s^{-1} (Figure 18).

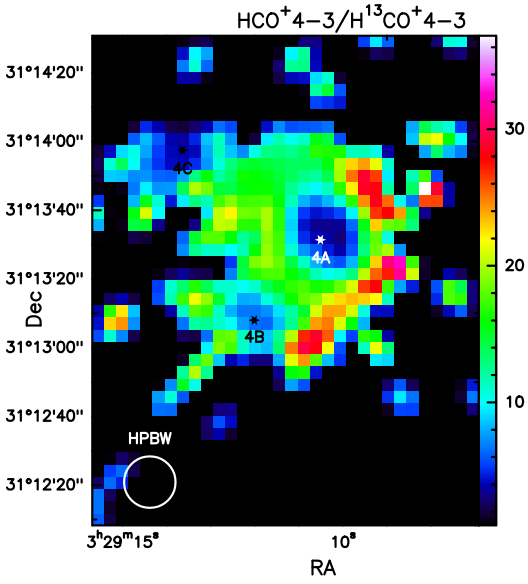

Fig. 18. Observed HCO^+ 4-3 / $H^{13}CO^+$ 4-3 ratio of the peak intensities for the range from +5 to +9 km s^{-1}. The fact that the observed ratio takes values between 6 and 37, which is smaller than the optically thin ratio of 60, indicates that the main isotope HCO^+ 4-3 is optically thick throughout the cloud. The effect is stronger towards the 3 embedded objects.

The observed ratio is found to vary between 6 and 37, which is 10 to 1.5 times smaller than the expected ratio of 60 under optically thin conditions, indicating that the main isotope HCO^+ 4-3 is moderately optically thick throughout the cloud. The effect is stronger towards the 3 embedded objects as expected. For this reason we produce the [DCO^+] / [HCO^+] towards the 3 sources using a fixed isotopic ratio of [HCO^+]/[$H^{13}CO^+$] = 60. We reran our calculations adopting the volume densities for each source as determined in Sec. 4.3 and we determine deuteration of ∼12±2% towards IRAS 4A, ∼3.5±1% towards IRAS 4B and an upper limit of ∼20% towards IRAS 4C. The lowest deuteration is towards IRAS 4B and is correlated also with the lower degree of depletion towards that source as we determine in Sec. 4.4. For IRAS 4C the error is an order of magnitude higher compared to the other 2 sources, since at such low temperatures a decrease or increase of temperature by only 5 K causes almost one order and half order of magnitude higher or lower N(DCO^+) and N(HCO^+) respectively. One would expect that IRAS 4C would show the higher degree of deuteration since it is the coldest among the sources and thus the enhancement of H_2D^+ abundance contributes to the enhancement of DCO^+ through the reaction $H_2D^+ + CO \Longrightarrow DCO^+ + H_2$. Although we report the highest deuteration towards IRAS 4C, this value is only an upper limit and we cannot draw safe conclusions regarding its evolutionary status compared to the other two sources only based on their deuteration.

4.6. HCN/HNC

We want to test our temperature estimates by using a method not connected to the H_2CO lines. The [HCN]/[HNC] ratio has been found to be sensitive to temperature (Schilke et al. 1992), while for cold molecular clouds is expected to be ∼1 (Sarrasin et al. 2010). More precisely HNC/HCN have been found to be decreasing while temperature increases and vice versa (Graninger et al. 2014).

We follow similar procedure as in Sec. 4.5 using the collisional rate coefficients for HCN and HNC from Dumouchel et al. (2010), scaled by a factor 1.37 to represent collisions with H_2. We use the optically thin $H^{13}CN$ and adopting a HCN/$H^{13}CN$ = 60 we present the observed HCN/HNC ratio towards the 3 sources. We find a ratio of ∼3.5 for IRAS 4A and ∼4.2 for IRAS 4B. The isotopologue $HN^{13}C$ did not show a clear detection and thus we assume that HNC is optically thin towards all 3 positions. None of the rarer isotopologues are observed towards IRAS 4C so we assume that the main isotopologues are optically thin and we find there the lowest observed ratio of ∼0.85.

Our results show nicely the correlation between HCN/HNC and the temperature, since the lowest value corresponds to the colder source (4C) and the highest to the warmer source (4B). We also find more HNC than HCN towards IRAS 4C, where the temperature is as low as ∼12 K and HNC emission is expected to be higher than HCN for such low temperatures (Padovani et al. 2011; Graninger et al. 2014).

5. Discussion and Conclusions

IRAS 4C, has been reported based on continuum observations in various previous works as a Class 0 object (e.g.; Enoch et al. 2009). We take the advantage of the direct comparison with the other 2 nearby Class 0 objects, IRAS 4A and IRAS 4B, using single dish mapping observations as they have been obtained during the JCMT line survey. In addition we report the mass and the volume density as was determined using our CARMA observations.

5.1. Results

We tried to distinguish the evolutionary stage of IRAS 4C compared to the other two Class 0 objects, taking into account the derived physical parameters from our analysis sections, the projection effects, the mass and the luminosity of the sources.

- We do not observe extended bipolar emission from the outflow towards IRAS 4C, as we would expect from an edge–on disk structure. IRAS 4A drives the faster outflow, followed by IRAS 4B and IRAS 4C. Outflows could be used as evolutionary constraints in the earlier phases of star formation.
- We determine the lowest kinetic temperature towards IRAS 4C (∼12 K), followed by IRAS 4A (∼45 K) and IRAS 4B (∼80 K).
- We take into account the different derived temperatures among the sources and we find IRAS 4C to have 3 times higher mass than IRAS 4B. This can explain why the line profile of $C^{17}O$ is stronger towards IRAS 4C than IRAS 4B. IRAS 4A remains the most massive among the sources (2 $M_\odot$).
- The warmest source IRAS 4B is characterized by the lowest degree of depletion and deuteration, and the highest HCN/HNC confirming its warm nature. In addition IRAS 4C is characterized by the highest degree of depletion and HCN/HNC < 1 characteristic of objects with very low temperature. Due to large errors at such low temperatures, we can only provide an upper limit for the deuteration towards IRAS 4C (∼20%).
- IRAS 4A is ∼2 times less warm, ∼3 times more massive with ∼4 times stronger outflow activity and ∼3 times lower deuteration than IRAS 4B, and it is probably younger than IRAS 4B.
- Our velocity distribution maps of several species show that IRAS 4A and IRAS 4B appear at different velocity from most of the region (+6.7 km s^{-1}), while IRAS 4C and the surrounding area peak at about 1 km s^{-1} higher velocity (+7.9 km s^{-1}). The observed absorption of the HCN profiles at +7.84 km s^{-1} can be an indicator that IRAS 4C may not be member of IRAS 4 cloud, but probably in foreground. Our analysis is not dependent on the distance though, with the exception of the mass calculation.

5.2. Discussion

Our JCMT data alone have revealed differences between the 3 sources that make us reconsider the true nature of IRAS 4C. The major differences appear in the: a) chemical composition (i.e. the spectrum of IRAS 4C appears less rich than the other two), b) the spatial distribution of some species are more extended towards IRAS 4A and IRAS 4B indicating stronger outflow activity, c) the line profiles suggest weak or non–existent outflow activity in IRAS 4C.

Moreover, the H_2CO kinetic temperature analysis reveals that IRAS 4C is characterized by the lowest kinetic temperature (∼12 K), followed by IRAS 4A (∼45 K) and IRAS 4B (∼80 K). HCN/HNC and DCO^+/HCO^+ ratios support the temperatures estimated from the H_2CO analysis. Furthermore, we determine the degree of CO depletion (N(CO)/N(H_2)) and deuteration (N(DCO^+)/N(HCO^+)) for each object. We determine the lowest degree of depletion to be towards IRAS 4B where the deuter-

ation is lower. We report values of 12% for IRAS 4A source, 3.5% for IRAS 4B, and an upper limit of 20% for IRAS 4C. Lastly, we find the [HCN]/[HNC] of ∼3.5 for IRAS 4A, ∼4.2 for IRAS 4B and ∼0.85 for IRAS 4C, being in agreement with the temperatures of the 3 sources.

We clearly observe differences between IRAS 4A, IRAS 4B and IRAS 4C, which may be due to (a) differences in mass and/or luminosity (b) a different orientation (edge–on vs face–on) or (c) evolution.

Previous studies report L_{bol} of 4.2 $L_{\odot}$, 1.6 $L_{\odot}$, 0.49 $L_{\odot}$ and M_{env} of 7.75 $M_{\odot}$, 3.66 $M_{\odot}$ and 0.5 $M_{\odot}$ for IRAS 4A, IRAS 4B and IRAS 4C respectively as detemined for a temperature of ∼ 50 K (Enoch et al. 2009). We estimate masses of ∼2 $M_{\odot}$ for IRAS 4A, 0.6 $M_{\odot}$ for IRAS 4B and 1.5 $M_{\odot}$ for IRAS 4C, using different temperatures for each source as determined in Sec. 4.2. The mass of the envelope shows a linear correlation with the luminosity of CO lines (San José-García et al. 2013). The fact that $C^{17}O$ emission towards IRAS 4C is stronger than IRAS 4B can be explained by the fact that we find ∼3 times higher mass towards IRAS 4C compared to IRAS 4B. The low bolometric luminosity towards IRAS 4C can be the main reason that we observe the weaker lines towards this source.

Dunham et al. (2008) report $L_{IR} = 0.305L_{\odot}$ for IRAS 4C as integrated for all existing detections between the 1.25–70 μm that corresponds to an internal luminosity $L_{INT} = 0.51L_{\odot}$ and excludes IRAS 4C from being a VeLLO since its luminosity is $> 0.1L_{\odot}$.

We finally see an emission from a fourth source, that we call IRAS 4–SWC in this work, the nature of which is not clear. IRAS 4–SWC shows line peaks at lower velocity (∼ 5.3km s^{-1}) and only narrow lines (∼3km s^{-1}) which can be either a projection effect of the outflow, or an indication that IRAS 4–SWC is a separate core. The non-detected emission at mid– and far– infrared at this position, while Winston et al. (2010) reports X–ray emission close to it, in combination with the fact that IRAS 4–SWC can be observed mostly in outflow tracers such as CH_3OH makes it unlike to be a separate core and connects it more with internal shock from the IRAS 4A outflow.

5.3. Younger age scenario

We start with investigating the scenario that IRAS 4C is in younger age than the other two objects.

A lower temperature can be an indication of earlier evolutionary state as soon as the objects of comparison are characterized by the same luminosity. This is not the case for our sources and thus we cannot base our interpretation on the kinetic temperature alone. The deuteration ($[N_2D^+]/[N_2H^+]$) has been measured from Crapsi et al. (2005a) to be ∼ 16 – 23 % for a prestellar core (e.g. L1544) and ∼ 5 – 10 % for Class 0 objects (e.g. L1521F). Our results suggest that IRAS 4C is not the source with the higher deuteration as expected for younger sources but our big errors towards IRAS 4C (16%) do not allow us to clearly distinguish it from the other two sources.

The bolometric temperature can be additionally used to probe the various evolutionary stages from prestellar core to protostars (e.g.; Enoch et al. 2009). Prestellar cores are characterized by T_{bol} ∼ 10–20 K while T_{bol} < 50 K can be used to classify an object as early Class 0. The reported values for IRAS 4A and IRAS 4B are ∼30–36 K (e.g.; Kristensen et al. 2012; Motte & André 2001) while for IRAS 4C T_{bol} = 26 K (Dunham et al. 2008). Enoch et al. (2009) reports a value of ∼ 50K for all 3 objects. The variations between the reported values in different studies make the use of T_{bol} alone not reliable enough to discriminate between the relative states of the sources.

Gutermuth et al. (2008) report IRAS 4C as a deeply embedded source with incomplete IRAC photometry but a relatively bright MIPS 24 μm. IRAS 4A shows compact point–like emission already at 3.6 μm and IRAS 4B at 4.5 μm (Young et al. 2015) being associated with shock knots, while IRAS 4C shows a more extended weaker emission at 8 μm. This information tells us that IRAS 4C possibly contains a compact hydrostatic object that can result in warm dust to emit at 8 and 24 μm, excluding IRAS 4C from being a pre–stellar core (>70 μm).

3–D radiation magneto–hydrodynamics simulations that reproduce the stage of a dense core collapse (Machida et al. 2008; Tomida et al. 2010) show that a slow poorly collimated outflow can exist, without the presence of a protostar, but rather due to the already formed FHSC. These simulations predict a very slow collimated outflow that does not exceed the velocity of 3 km s^{-1}. On the other hand, both theory and observations (Shang 2007; Arce & Sargent 2006), report highly collimated outflows from YSOs that reach velocities up to a few tens of km s^{-1}. IRAS 4C does not seem to drive a strong outflow, while IRAS 4A and IRAS 4B do show a strong outflow activity (high velocity gas). The orientation plays an important role when it comes to the observed outflow. Line emission from outflow tracers such as CO, is more sensitive to the different orientation of the sources and can affect the strenght of the observed outflow. Thus the observed differences in the outflow activity could be a result of a) orientation and/or b) evolution.

Although the orientation of the source may influence the interpretation of the outflow emission, it does not affect the estimated values of the degrees of CO depletion and deuteration. $C^{17}O$, DCO^+ and HCO^+ are all species found to trace the envelope. Given the fact that the single dish observations cannot resolve a disk structure, we assume that all of the observed emission comes from the bulk of gas tracing the envelope and thus it is independent of the orientation of the sources. The determined values towards IRAS 4C, point towards a colder, less evolved source compared to IRAS 4A and IRAS 4B, either between the prestellar and protostellar phase (FHSC) or a very young Class 0 object at the earliest accretion phase which makes it one of the very few observed cases (e.g.; André et al. 1999; Belloche et al. 2006).

5.4. Older age scenario

We now investigate the scenario that IRAS 4C is in an older age than the other two objects.

Tobin et al. (2015) & Segura–Cox et al. 2015 (submitted) report strong evidence of an edge on disk–like structure around IRAS 4C, although the S/N in that work was not sufficient to test for Keplerian rotation. A disk–structure indicates that IRAS 4C is a more evolved object than a FHSC, probably an object in the transition phase between Class 0 and Class I. An edge on disk–like structure can cause an underestimation of the observed T_{bol} by even ∼100 K (Launhardt et al. 2013). This would favor the scenario that IRAS 4C is actually a more evolved object with T_{bol}>70 K, bringing it closer to the late Class 0 to early Class I stage. This would also be in agreement with the fact that IRAS 4C is the object with the lowest luminosity, which might indicate less strong accreting activity and thus a more evolved object. Another indicator of evolutionary stage is the ratio L_{smm}/L_{bol} which is expected to be higher the less evolved the object is, and it is considered to be more accurate than T_{bol}. This was found to be 5% for IRAS 4A, 5.5% for IRAS 4B and

6.3% for IRAS 4C (Dunham et al. 2008; Sadavoy et al. 2014). Launhardt et al. (2013) report values of 3%<L_{smm}/L_{bol}<7% for Class 0 and Class I objects, while Andre et al. (2000) had previously proposed a threshold of <0.3% for Class I objects. Furthermore they report 10%<L_{smm}/L_{bol}<30% for starless cores and objects that could possibly host an embedded FHSC. This could limit the classification of IRAS 4C as FHSC, but the reported values for the 3 sources are close enough, making it difficult to distinguish between the Class 0 and Class I stage. A rough classification would bring IRAS 4C to the Class 0 stage but probably younger than the other two.

The collimation and bipolarity of an outflow can be used to distinguish Class 0 objects from the more evolved Class I objects. For Class I objects the outflow angle is wider and as we move further to the evolution, the swept–up material is slowing down, since the driving force is reducing (Arce & Sargent 2006). Outflows in Class 0 sources have proven to be much stronger than in Class I objects (Bontemps et al. 1996).

Our CARMA observations indicate the presence of a slow outflow (~2km s^{-1}) which is not characterized by a wide angle and it is rather compact. The nebulosity revealed by Spitzer shows a scattered light cone which has an origin at the location of the protostar indicating that the most likely direction of the outflow is orthogonal to the plane of the disk. The edge on disk scenario can explain the apparent low outflow velocity and thus partially why the line profiles from JCMT are so narrow towards IRAS 4C and deprived of the higher velocity activity but it cannot explain that we do not observe spatially an extended outflow. The relatively wide cone–like structure to the east of IRAS 4C which is observed in our CO maps from JCMT, could be connected to the outflow activity. There is the possibility that we do not observe similar structure to the west of IRAS 4C, due to the strong interaction with the red lobe of IRAS 4A. A more powerful outflow from 4A would sweep the red lobe of IRAS 4C away, but this requires a very specific geometry and distance of the sources and the outflows. This is the only scenario that can explain the observed outflow by an older age object, but the difference in $V_{\rm LSR}$ argues against it. Also, this explanation cannot be valid if IRAS 4C is a foreground object, since there is no way for the outflow lobes to interact.

On the other hand, an outflow parallel to our line of sight could explain a more compact outflow but that would mean that the observed velocity is very close to the real velocity and thus very slow, and thus inconsistent with an older age.

5.5. Conclusions and future direction

Neither the younger nor the older age scenario seems to be fully consistent with the body of observational data on IRAS 4C. If IRAS 4C is old enough to reveal a disk structure, we cannot fully explain the missing outflow, and the cold nature of the source. If IRAS 4C is so young that cannot drive a powerful outflow, we cannot explain the low L_{smm}/L_{bol} and the disk structure that has previously been observed. IRAS 4C appears not to be the strongest candidate among the FHSC candidates. Nevertheless, if all of the candidates located in Perseus (e.g.; Pezzuto et al. 2012; Enoch et al. 2010) will be confirmed, while statistics predict < 0.2, it would be a strong evidence that the lifespan of these objects is $\geq 10^3$ years. This can be a result of a lower mass accretion rate (<$4\times10^{-5} M_{\odot}$/yr) or that special conditions apply to Perseus, perhaps a non–stationary accretion. Tomida et al. (2010) predict a lifespan longer than 10^4 yrs for a protostar of $0.1 M_{\odot}$ adopting an accretion rate of $10^{-5} M_{\odot}$/yr and this would improve the situation in Perseus by an order of magnitude.

Applying FHSC and YSO disk models towards IRAS 4C will help us characterizing more accurately this object. In addition, the detailed study of the outflow of the observed FHSCs and VeLLOs may be helpful in understanding the missing link between these early stages of star formation.

Acknowledgements. The authors thank Mark Krumholz for useful discussions. J.J.T. is supported by grant 639.041.439 from the Netherlands Organisation for Scientific Research (NWO).

References

André, P., Motte, F., & Bacmann, A. 1999, ApJ, 513, L57
Andre, P., Ward-Thompson, D., & Barsony, M. 2000, Protostars and Planets IV, 59
Arce, H. G. & Sargent, A. I. 2006, ApJ, 646, 1070
Arce, H. G., Shepherd, D., Gueth, F., et al. 2007, Protostars and Planets V, 245
Bacmann, A., André, P., Puget, J.-L., et al. 2000, A&A, 361, 555
Bacmann, A., Lefloch, B., Ceccarelli, C., et al. 2002, A&A, 389, L6
Bacmann, A., Lefloch, B., Ceccarelli, C., et al. 2003, ApJ, 585, L55
Belloche, A., Parise, B., van der Tak, F. F. S., et al. 2006, A&A, 454, L51
Bergin, E. A. & Tafalla, M. 2007, ARA&A, 45, 339
Beuther, H., Semenov, D., Henning, T., & Linz, H. 2008, ApJ, 675, L33
Blake, G. A., Sandell, G., van Dishoeck, E. F., et al. 1995, ApJ, 441, 689
Bontemps, S., Andre, P., Terebey, S., & Cabrit, S. 1996, A&A, 311, 858
Bourke, T. L., Myers, P. C., Evans, II, N. J., et al. 2006, ApJ, 649, L37
Buckle, J. V., Hills, R. E., Smith, H., et al. 2009, MNRAS, 399, 1026
Caselli, P., Walmsley, C. M., Tafalla, M., Dore, L., & Myers, P. C. 1999, ApJ, 523, L165
Chen, X., Arce, H. G., Zhang, Q., et al. 2010, ApJ, 715, 1344
Choi, M., Kamazaki, T., Tatematsu, K., & Panis, J.-F. 2004, ApJ, 617, 1157
Crapsi, A., Caselli, P., Walmsley, C. M., et al. 2005a, ApJ, 619, 379
Crapsi, A., Devries, C. H., Huard, T. L., et al. 2005b, A&A, 439, 1023
Di Francesco, J., Myers, P. C., Wilner, D. J., Ohashi, N., & Mardones, D. 2001, ApJ, 562, 770
Duarte-Cabral, A., Bontemps, S., Motte, F., et al. 2014, A&A, 570, A1
Dumouchel, F., Faure, A., & Lique, F. 2010, MNRAS, 406, 2488
Dunham, M. M., Crapsi, A., Evans, II, N. J., et al. 2008, ApJS, 179, 249
Dunham, M. M., Evans, II, N. J., Bourke, T. L., et al. 2006, ApJ, 651, 945
Elitzur, M., Hollenbach, D. J., & McKee, C. F. 1992, ApJ, 394, 221
Enoch, M. L., Evans, II, N. J., Sargent, A. I., & Glenn, J. 2009, ApJ, 692, 973
Enoch, M. L., Evans, II, N. J., Sargent, A. I., et al. 2008, ApJ, 684, 1240
Enoch, M. L., Lee, J.-E., Harvey, P., Dunham, M. M., & Schnee, S. 2010, ApJ, 722, L33
Enoch, M. L., Young, K. E., Glenn, J., et al. 2006, ApJ, 638, 293
Evans, II, N. J., Allen, L. E., Blake, G. A., et al. 2003, PASP, 115, 965
Evans, II, N. J., Dunham, M. M., Jørgensen, J. K., et al. 2009, ApJS, 181, 321
Flower, D. R. 1999, MNRAS, 305, 651
Fontani, F., Palau, A., Caselli, P., et al. 2011, A&A, 529, L7
Fontani, F., Sakai, T., Furuya, K., et al. 2014, MNRAS, 440, 448
Friesen, R. K., Kirk, H. M., & Shirley, Y. L. 2013, ApJ, 765, 59
Furuya, R. S., Kitamura, Y., Wootten, A., Claussen, M. J., & Kawabe, R. 2003, ApJ, 144, 71
Graninger, D. M., Herbst, E., Öberg, K. I., & Vasyunin, A. I. 2014, ApJ, 787, 74
Green, S. 1991, ApJS, 76, 979
Gregersen, E. M. & Evans, II, N. J. 2000, ApJ, 538, 260
Gutermuth, R. A., Myers, P. C., Megeath, S. T., et al. 2008, ApJ, 674, 336
Haschick, A. D., Moran, J. M., Rodriguez, L. F., et al. 1980, ApJ, 237, 26
Hatchell, J., Richer, J. S., Fuller, G. A., et al. 2005, A&A, 440, 151
Herbig, G. H. & Jones, B. F. 1983, AJ, 88, 1040
Hirota, T., Bushimata, T., Choi, Y. K., et al. 2008, PASJ, 60, 37
Jørgensen, J. K., Harvey, P. M., Evans, II, N. J., et al. 2006, ApJ, 645, 1246
Kristensen, L. E., van Dishoeck, E. F., Bergin, E. A., et al. 2012, A&A, 542, A8
Langer, W. D., Castets, A., & Lefloch, B. 1996, ApJ, 471, L111
Larson, R. B. 1969, MNRAS, 145, 271
Launhardt, R., Stutz, A. M., Schmiedeke, A., et al. 2013, A&A, 551, A98
Lee, C. W., Kim, M.-R., Kim, G., et al. 2013, ApJ, 777, 50
Lee, K. I., Dunham, M. M., Myers, P. C., et al. 2015, ApJ, 814, 114
Lefloch, B., Castets, A., Cernicharo, J., & Loinard, L. 1998, ApJ, 504, L109
Linsky, J. L., Diplas, A., Wood, B. E., et al. 1995, ApJ, 451, 335
Looney, L. W., Mundy, L. G., & Welch, W. J. 2000, ApJ, 529, 477
Machida, M. N. & Hosokawa, T. 2013, MNRAS, 431, 1719
Machida, M. N., Matsumoto, T., & Inutsuka, S.-i. 2008, ApJ, 685, 690
Maret, S., Bergin, E. A., Neufeld, D. A., et al. 2009, ApJ, 698, 1244
Maret, S., Ceccarelli, C., Caux, E., et al. 2004, A&A, 416, 577
Marvel, K. B., Wilking, B. A., Claussen, M. J., & Wootten, A. 2008, ApJ, 685, 285

Millar, T. J., Bennett, A., & Herbst, E. 1989, ApJ, 340, 906
Motte, F. & André, P. 2001, A&A, 365, 440
Ossenkopf, V. & Henning, T. 1994, A&A, 291, 943
Padovani, M., Walmsley, C. M., Tafalla, M., Hily-Blant, P., & Pineau Des Forêts, G. 2011, A&A, 534, A77
Pagani, L., Lesaffre, P., Jorfi, M., et al. 2013, A&A, 551, A38
Parise, B., Ceccarelli, C., Tielens, A. G. G. M., et al. 2006, A&A, 453, 949
Park, G. & Choi, M. 2007, ApJ, 664, L99
Pezzuto, S., Elia, D., Schisano, E., et al. 2012, A&A, 547, A54
Pickett, H. M., Poynter, R. L., Cohen, E. A., et al. 1998, J. Quant. Spec. Radiat. Transf., 60, 883
Pineda, J. E., Arce, H. G., Schnee, S., et al. 2011, ApJ, 743, 201
Plume, R., Fuller, G. A., Helmich, F., et al. 2007, PASP, 119, 102
Rodríguez, L. F., Anglada, G., Torrelles, J. M., et al. 2002, A&A, 389, 572
Sadavoy, S. I., Di Francesco, J., André, P., et al. 2014, ApJ, 787, L18
Sakai, N., Saruwatari, O., Sakai, T., Takano, S., & Yamamoto, S. 2010, A&A, 512, A31
San José-García, I., Mottram, J. C., Kristensen, L. E., et al. 2013, A&A, 553, A125
Sandell, G. & Knee, L. B. G. 2001, ApJ, 546, L49
Santangelo, G., Codella, C., Cabrit, S., et al. 2015, ArXiv e-prints
Sarrasin, E., Abdallah, D. B., Wernli, M., et al. 2010, MNRAS, 404, 518
Sault, R. J., Teuben, P. J., & Wright, M. C. H. 1995, in Astronomical Society of the Pacific Conference Series, Vol. 77, Astronomical Data Analysis Software and Systems IV, ed. R. A. Shaw, H. E. Payne, & J. J. E. Hayes, 433
Schilke, P., Walmsley, C. M., Pineau Des Forets, G., et al. 1992, A&A, 256, 595
Schnee, S., Sadavoy, S., Di Francesco, J., Johnstone, D., & Wei, L. 2012, ApJ, 755, 178
Schöier, F. L., van der Tak, F. F. S., van Dishoeck, E. F., & Black, J. H. 2005, A&A, 432, 369
Shah, R. Y. & Wootten, A. 2001, ApJ, 554, 933
Shang, H. 2007, Ap&SS, 311, 25
Smith, K. W., Bonnell, I. A., Emerson, J. P., & Jenness, T. 2000, MNRAS, 319, 991
Tobin, J. J., Bergin, E. A., Hartmann, L., et al. 2013, ApJ, 765, 18
Tobin, J. J., Looney, L. W., Wilner, D. J., et al. 2015, ApJ, 805, 125
Tomida, K., Machida, M. N., Saigo, K., Tomisaka, K., & Matsumoto, T. 2010, ApJ, 725, L239
van der Tak, F. F. S., Black, J. H., Schöier, F. L., Jansen, D. J., & van Dishoeck, E. F. 2007, A&A, 468, 627
van Kempen, T. A., Hogerheijde, M. R., van Dishoeck, E. F., et al. 2006, A&A, 454, L75
Wiesenfeld, L. & Faure, A. 2013, MNRAS, 432, 2573
Wilson, T. L. 1999, Reports on Progress in Physics, 62, 143
Winston, E., Megeath, S. T., Wolk, S. J., et al. 2010, AJ, 140, 266
Wootten, A. 1995, Ap&SS, 224, 43
Yıldız, U. A., Kristensen, L. E., van Dishoeck, E. F., et al. 2012, A&A, 542, A86
Young, C. H., Jørgensen, J. K., Shirley, Y. L., et al. 2004, ApJS, 154, 396
Young, K. E., Young, C. H., Lai, S.-P., Dunham, M. M., & Evans, II, N. J. 2015, AJ, 150, 40

Appendix A: Line detections towards the 3 sources

Table A.1. Molecular Line Detections for NGC 1333-IRAS 4A - JCMT data

				Broad	**component**		**Narrow**	**component**	
Molecule	Transition	Rest Frequency (MHz)	E_{up} (K)	V_{lsr} (km s^{-1})	FWHM (km s^{-1})	T_A^* (K)	V_{lsr} (km s^{-1})	FWHM (km s^{-1})	T_A^* (K)
HCN	4-3	354505.5	42.5	5.03 ± 0.21	13.7 ± 0.5	0.67 ± 0.03			
$H^{13}CN$	4-3	345339.8	41.4	6.4 ± 0.7	14 ± 2	0.04 ± 0.01	7.8 ± 0.3	2.8 ± 1.0	0.03 ± 0.01
HNC	4-3	362630.3	43.5	7.66 ± 0.05	1.18 ± 0.08	1.26 ± 0.08			
CO	3-2	345796.0	33.2	9.2 ± 0.8	22.3 ± 2	2.6 ± 0.2	6.7 ± 0.1	1.5 ± 0.2	6.1 ± 0.7
^{13}CO	3-2	330588.0	31.7	7.3 ± 0.9	10 ± 3	0.4 ± 0.1	7.63 ± 0.05	2.1 ± 0.2	3.3 ± 0.2
$C^{17}O$	3-2	337061.1	32.4	7.65 ± 0.02	1.52 ± 0.06	0.70 ± 0.02			
HCO^+	4-3	356734.1	42.8	8.87 ± 0.55	10.2 ± 1.5	0.71 ± 0.09	7.41 ± 0.04	1.21 ± 0.08	3.43 ± 0.19
$H^{13}CO^+$	4-3	346998.3	41.6	7.64 ± 0.02	1.24 ± 0.04	0.87 ± 0.02			
$H_2{}^{13}CO$	5(1,5)-4(1,4)	343325.7	61.3	6.9 ± 0.4	3 ± 1	0.06 ± 0.2			
$H_2{}^{13}CO$	5(2,3)-4(2,2)	356176.2	98.5	8.0 ± 0.2	2.6 ± 0.7	0.06 ± 0.01			
CS	7-6	342882.8	65.8	6.53 ± 0.09	11.77 ± 0.25	0.69 ± 0.01	7.53 ± 0.02	1.26 ± 0.12	0.87 ± 0.05
$C^{34}S$	7-6	337396.7	50.2	7.1 ± 0.2	3.2 ± 0.5	0.16 ± 0.02			
H_2CS	10(1,10)-9(1,9)	338083.2	102.4	7.54 ± 0.52	7.0 ± 1.4	0.06 ± 0.01			
H_2CS	10(2,9)-9(2,8)	343322.1	143.3	4.3 ± 0.7	6.0 ± 1.7	0.04 ± 0.01			
H_2CS	10(1,9)-9(1,8)	348534.4	105.2	8.0 ± 0.6	5.1 ± 1.5	0.06 ± 0.01			
OCS	28-27	340449.2	237.0	7.6 ± 0.2	3.8 ± 0.6	0.054 ± 0.007			
CH_3OH	11(1,10)-11(0,11)	331502.3	169.0	4.6 ± 0.6	10.0 ± 1.4	0.06 ± 0.01	7.07 ± 0.47	2.29 ± 1.34	0.02 ± 0.01
CH_3OH	7(1,7)-6(1,6)	335582.0	79.0	5.1 ± 1.4	9.2 ± 3.0	0.04 ± 0.04	7.8 ± 1.5	2.7 ± 5.2	0.04 ± 0.04
CH_3OH	7(0,7)-6(0,6)	338124.5	78.1	5.5 ± 0.4	10.2 ± 0.9	0.12 ± 0.01	7.8 ± 0.2	1.0 ± 0.5	0.10 ± 0.03
CH_3OH	7(-1,7)-6(-1,6)	338344.6	70.6	5.3 ± 0.1	10.2 ± 0.2	0.27 ± 0.08	7.61 ± 0.05	2.16 ± 0.14	0.25 ± 0.01
CH_3OH	7(-1,7)-6(-1,6)++	338408.7	65.0	5.4 ± 0.2	10.3 ± 0.4	0.34 ± 0.02	7.48 ± 0.08	2.04 ± 0.22	0.29 ± 0.02
CH_3OH	7(2,6)-6(2,5)–	338512.9	102.7	7.2 ± 0.7	7.2 ± 1.8	0.04 ± 0.01			
CH_3OH	7(3,4)- 6(3,3)	338583.2	112.7	7.6 ± 0.2	2.6 ± 0.6	0.05 ± 0.01			
CH_3OH	7(3,5)-6(3,4)++	338540.8	114.8	5.9 ± 0.2	4.5 ± 0.5	0.07 ± 0.01			
CH_3OH	7(1,6)-6(1,5)	338615.0	86.0	7.8 ± 0.3	10.2 ± 0.9	0.08 ± 0.01	7.7 ± 0.1	1.7 ± 0.4	0.05 ± 0.01
CH_3OH	7(2,5)-6(2,4)	338721.7	87.3	6.1 ± 0.2	8.5 ± 0.5	0.14 ± 0.01	7.9 ± 0.2	2.0 ± 0.6	0.06 ± 0.01
CH_3OH	7(-2,5)-6(-2,4)	338722.9	90.9	7.1 ± 0.2	8.5 ± 0.5	0.14 ± 0.01	8.9 ± 0.2	2.1 ± 0.6	0.06 ± 0.01
CH_3OH	7(1,6)-6(1,5)–	341415.6	80.1	5.2 ± 0.3	8.2 ± 0.6	0.11 ± 0.01	7.2 ± 0.3	2.9 ± 1.0	0.05 ± 0.02
CH_3OH	13(1,12)-13(0,13)-+	342729.8	227.5	7.0 ± 1.0	8.5 ± 3.1	0.03 ± 0.01			
CH_3OH	4(0,4)-3(-1,3)	350687.7	36.3	4.8 ± 0.7	9.0 ± 1.4	0.09 ± 0.02	6.9 ± 0.2	2.7 ± 0.6	0.14 ± 0.02
CH_3OH	1(1,1)-0(0,0)++	350905.1	16.8	4.4 ± 1.2	7.3 ± 2.5	0.11 ± 0.03	6.9 ± 0.4	2.2 ± 1.2	0.13 ± 0.05
CH_3OH	4(1,3)-3(0,3)	358605.8	44.3	5.2 ± 0.5	8.7 ± 0.9	0.10 ± 0.01	7.4 ± 0.1	2.2 ± 0.4	0.12 ± 0.02
CH_3OH	8(1,7)-7(2,5)	361852.2	104.6	6.8 ± 0.4	4.7 ± 1.0	0.03 ± 0.001			
CH_3OH	7(2,5)-6(1,5)	363739.8	87.2	7.5 ± 0.9	11.4 ± 4.4	0.05 ± 0.02	7.3 ± 0.3	2.9 ± 1.3	0.06 ± 0.02
H_2CO	5(1,5)-4(1,4)	351768.6	62.4	6.0 ± 0.1	9.0 ± 0.4	0.71 ± 0.03	7.43 ± 0.03	1.41 ± 0.08	1.16 ± 0.05
H_2CO	5(0,5)-4(0,4)	362736.0	52.3	7.16 ± 0.09	9.1 ± 0.2	0.28 ± 0.01	7.81 ± 0.02	1.40 ± 0.07	0.53 ± 0.04
H_2CO	5(2,4)-4(2,3)	363945.9	99.5	6.49 ± 0.05	11.1 ± 0.1	0.08 ± 0.01	8.01 ± 0.01	1.94 ± 0.03	0.12 ± 0.01
H_2CO	5(2,3)-4(2,2)	365363.4	99.7	7.34 ± 0.08	8.5 ± 0.2	0.12 ± 0.02	8.25 ± 0.02	0.91 ± 0.05	0.15 ± 0.03
H_2CO	5(3,3)-4(3,2)	364275.1	158.4	7.0 ± 3.1	11.0 ± 4.8	0.09 ± 0.03	8.3 ± 0.2	1.8 ± 0.7	0.08 ± 0.02
H_2CO	5(3,2)-4(3,1)	364288.9	158.4	5.8 ± 1.9	12.4 ± 3.4	0.09 ± 0.01	7.6 ± 0.2	1.4 ± 0.5	0.08 ± 0.02
H_2CO	5(4,2)-4(4,1)	364103.2	240.7	9.0 ± 0.7	5.6 ± 1.9	0.04 ± 0.01			
DCO^+	5-4	360169.8	51.9	7.56 ± 0.02	1.11 ± 0.07	0.45 ± 0.02			
SO $^3\Sigma$	7(8)-6(7)	340714.2	81.2	5.2 ± 0.6	14.3 ± 1.5	0.10±0.01			
SO $^3\Sigma$	8(8)-7(7)	344310.6	87.5	5.2 ± 0.3	12.5 ± 0.8	0.118 ± 0.006			
SO $^3\Sigma$	8(9)-7(8)	346528.5	78.8	5.4 ± 0.3	14.5 ± 0.9	0.27 ± 0.01			
^{33}SO	10(11)-10(10)	332014.3	141.5	5.5 ± 0.1	4.0 ± 0.2	0.187 ± 0.008			
SO_2	4(3,1)-3(2,2)	332505.2	31.3	7.7 ± 0.7	5 ± 1	0.04 ± 0.01			
C_2H	N=4-3, J=9/2-7/2, F= 4-3	349337.5	41.9	7.8 ± 0.2	4.9 ± 0.5	0.09 ± 0.01			
C_2H	N=4-3, J=7/2-5/2, F= 4-3	349399.3	41.9	8.0 ± 0.7	5.4 ± 1.9	0.06 ± 0.01			
CN	N=3-2, J=5/2-3/2, F=7/2-5/2	340031.5	32.6	6.9 ± 1	5 ± 3	0.09 ± 0.03			
CN	N=3-2, J=7/2-5/2, F=9/2-7/2	340247.8	32.7	7.87 ± 0.05	1.5 ± 0.1	0.38 ± 0.02			
HDCO	5(1,4)-4(1,3)	335096.9	56.2	7.5 ± 0.2	1.1 ± 0.3	0.09 ± 0.02			
HDCO	6(1,6)-5(1,5)	369763.5	70.1	7.6 ± 0.2	1.0 ± 0.4	0.10 ± 0.03			
D_2CO	6(0,6)-5(0,5)	342522.1	58.1	7.7 ± 0.2	2.7 ± 0.8	0.08 ± 0.01			
SiO	8-7	347330.6	75.0	−0.5±1.7	24±6	0.04±0.01	4.4±0.5	4.7±1.5	0.05±0.01
N_2H^+	4-3	372672.5	44.7	7.52 ± 0.08	3.47 ± 0.34	0.41 ± 0.78	7.39 ± 0.05	1.0 ± 0.3	1.8 ± 0.7

Table A.2. Molecular Line Detections for NGC 1333-IRAS 4B - JCMT data

				Broad	**component**		**Narrow**	**component**	
Molecule	Transition	Rest Frequency (MHz)	E_{up} (K)	V_{lsr} (km s^{-1})	FWHM (km s^{-1})	T_A^* (K)	V_{lsr} (km s^{-1})	FWHM (km s^{-1})	T_A^* (K)
HCN	4-3	354505.5	42.5	8.0 ± 0.2	11.5 ± 0.5	1.04 ± 0.05	7.11 ± 0.04	0.9 ± 0.8	1.2 ± 1
$H^{13}CN$	4-3	345339.8	41.4	8.4 ± 0.3	7.1 ± 0.8	0.08 ± 0.01			
HNC	4-3	362630.3	43.5	7.8 ± 0.2	4.5 ± 0.6	0.12 ± 0.02	7.67 ± 0.02	1.09 ± 0.04	0.89 ± 0.03
CO	3-2	345796.0	33.2	9.3 ± 0.4	14.6 ± 1.0	1.2 ± 0.1	6.78 ± 0.04	1.8 ± 0.1	4.2 ± 0.2
^{13}CO	3-2	330587.9	31.7	7.90 ± 0.03	2.56 ± 0.08	2.8 ± 0.1			
$C^{17}O$	3-2	337061.1	32.4	7.4 ± 0.1	1.8 ± 0.1	0.37 ± 0.03			
HCO^+	4-3	356734.1	42.8	9.5 ± 0.4	9.9 ± 0.9	0.45 ± 0.04	7.47 ± 0.03	1.36 ± 0.07	2.1 ± 0.1
$H^{13}CO^+$	4-3	346998.3	41.6	7.70 ± 0.05	1.26 ± 0.09	0.35 ± 0.02			
$H_2{}^{13}CO$	5(1,5)-4(1,4)	343325.7	61.3	8.3 ± 0.2	1.6 ± 0.3	0.11 ± 0.02			
CS	7-6	342882.8	65.8	8.0 ± 0.1	10.5 ± 0.2	0.63 ± 0.02	7.86 ± 0.03	2.6 ± 0.1	0.77 ± 0.03
CH_3OH	11(1,10)-11(0,11)	331502.4	169.0	8.5 ± 0.5	9.6 ± 2.2	0.08 ± 0.03	8.0 ± 0.1	3.5 ± 0.6	0.15 ± 0.03
CH_3OH	7(1,7)-6(1,6)	335582.0	79.0	8.3 ± 0.2	5.3 ± 0.4	0.18 ± 0.02	7.4 ± 0.1	1.3 ± 0.3	0.14 ± 0.03
CH_3OH	12(1,11)-12(0,12)	336865.1	197.1	8.5 ± 0.1	4.8 ± 0.4	0.14 ± 0.01			
CH_3OH	7(0,7)-6(0,6)	338124.5	78.1	9.3 ± 0.4	7.2 ± 0.7	0.15 ± 0.02	7.78 ± 0.09	2.2 ± 0.3	0.27 ± 0.03
CH_3OH	7(-1,6)-6(-1,6)	338344.6	70.5	8.8 ± 0.1	7.0 ± 0.4	0.34 ± 0.03	7.81 ± 0.04	2.2 ± 0.1	0.58 ± 0.03
CH_3OH	7(6,2)-6(6,1) -	338404.6	243.8	5.2 ± 0.2	7.3 ± 0.4	0.39 ± 0.04	4.16 ± 0.05	2.1 ± 0.2	0.67 ± 0.04
CH_3OH	7(-1,7)-6(-1,6)++	338408.7	65.0	8.8 ± 0.2	7.3 ± 0.4	0.38 ± 0.04	7.79 ± 0.05	2.2 ± 0.1	0.67 ± 0.04
CH_3OH	7(2,6)-6(2,5)–	338512.9	102.7	8.5 ± 0.1	3.6 ± 0.2	0.13 ± 0.01			
CH_3OH	7(3,5)-6(3,4)++	338540.8	114.8	7.5 ± 0.1	5.0 ± 0.3	0.15 ± 0.01			
CH_3OH	7(3,4)- 6(3,3)	338583.2	112.7	8.6 ± 0.4	2.9 ± 0.8	0.06 ± 0.01			
CH_3OH	7(1,6)-6(1,5)	338615.0	86.0	9.2 ± 0.4	6.8 ± 0.8	0.12 ± 0.02	7.9 ± 0.1	1.9 ± 0.4	0.17 ± 0.03
CH_3OH	7(2,5)-6(2,4)++	338639.9	102.7	8.4 ± 0.2	4.8 ± 0.6	0.08 ± 0.01			
CH_3OH	7(2,5)-6(2,4)	338721.6	87.3	11.8 ± 0.8	4.1 ± 1.4	0.09 ± 0.02	7.7 ± 0.16	3.8 ± 0.2	0.45 ± 0.02
CH_3OH	7(1,6)-6(1,5)–	341415.6	80.1	8.9 ± 0.2	6.3 ± 0.4	0.18 ± 0.02	7.78 ± 0.05	2.1 ± 0.2	0.31 ± 0.02
CH_3OH	13(1,12)-13(0,13)-+	342729.8	227.5	8.6 ± 0.3	6.3 ± 0.6	0.11 ± 0.02	7.3 ± 0.3	1.9 ± 0.8	0.06 ± 0.02
CH_3OH	4(0,4)-3(-1,3)	350687.7	36.3	8.3 ± 0.2	5.7 ± 0.6	0.15 ± 0.02	7.49 ± 0.07	1.7 ± 0.2	0.23 ± 0.03
CH_3OH	1(1,1)-0(0,0)++	350905.1	16.8	8.8 ± 0.3	6.0 ± 0.5	0.16 ± 0.02	7.48 ± 0.05	1.3 ± 0.3	0.28 ± 0.03
CH_3OH	13(0,13)-12(1,12)++	355603.1	211.0	8.6 ± 0.3	5.7 ± 0.8	0.14 ± 0.02			
CH_3OH	4(1,3)-3(0,3)	358605.8	44.3	8.0 ± 0.2	4.7 ± 0.7	0.18 ± 0.06	7.8 ± 0.1	1.7 ± 0.4	0.20 ± 0.06
CH_3OH	11(0,11)-10(1,9)	360848.9	166.0	8.3 ± 0.2	6.6 ± 0.7	0.05 ± 0.01	8.0 ± 0.2	1.2 ± 1.0	0.02 ± 0.01
CH_3OH	8(1,7)-7(2,5)	361852.2	104.6	7.9 ± 0.6	7.2 ± 1.9	0.05 ± 0.01	7.5 ± 0.1	0.9 ± 3.2	0.08 ± 0.30
CH_3OH	7(2,5)-6(1,5)	363739.8	87.2	8.7 ± 0.2	6.8 ± 0.6	0.16 ± 0.02	8.06 ± 0.06	1.7 ± 0.2	0.25 ± 0.02
H_2CO	5(1,5)-4(1,4)	351768.6	62.4	8.7 ± 0.2	8.2 ± 0.5	0.66 ± 0.07	7.60 ± 0.03	2.6 ± 0.1	1.81 ± 0.07
H_2CO	5(0,5)-4(0,4)	362736.0	52.3	7.9 ± 0.03	2.2 ± 0.1	1.17 ± 0.04	7.86 ± 0.03	2.25 ± 0.09	1.17 ± 0.04
H_2CO	5(2,4)-4(2,3)	363945.8	99.5	8.4 ± 0.1	5.1 ± 0.4	0.27 ± 0.04	7.94 ± 0.06	1.9 ± 0.2	0.33 ± 0.04
H_2CO	5(2,3)-4(2,2)	365363.4	99.7	9.1 ± 0.3	9.0 ± 0.9	0.13 ± 0.02	8.33 ± 0.04	2.6 ± 0.2	0.48 ± 0.02
H_2CO	5(3,3)-4(3,2)	364275.1	158.4	8.7 ± 0.5	7.5 ± 1.1	0.18 ± 0.04	8.16 ± 0.08	2.5 ± 0.3	0.36 ± 0.04
H_2CO	5(3,2)-4(3,1)	364288.9	158.4	9.4 ± 0.9	7.9 ± 2.0	0.16 ± 0.04	8.16 ± 0.07	2.7 ± 0.3	0.40 ± 0.05
H_2CO	5(4,2)-4(4,1)	364103.25	240.7	8.5 ± 0.2	3.9 ± 0.4	0.11 ± 0.01			
DCO^+	5-4	360169.8	51.9	7.65 ± 0.09	0.8 ± 0.4	0.6 ± 0.3			
SO $^3\Sigma$	3(3)-3(2)	339341.5	25.5	8.5 ± 0.1	1.3 ± 0.2	0.16 ± 0.02			
SO $^3\Sigma$	7(8)-6(7)	340714.2	81.2	8.2 ± 0.4	7.8 ± 1.1	0.07 ± 0.01	7.1 ± 0.2	1.3 ± 0.6	0.06 ± 0.02
SO $^3\Sigma$	8(8)-7(7)	344310.61	87.5	9.4 ± 0.5	10.1 ± 1.1	0.06 ± 0.01	7.6 ± 0.1	1.9 ± 0.6	0.06 ± 0.02
SO $^3\Sigma$	9(8)-8(7)	346528.5	78.8	9.5 ± 0.4	12.7 ± 0.9	0.10 ± 0.01	7.8 ± 0.1	2.4 ± 0.3	0.13 ± 0.01
SO_2	4(3,1)-3(2,2)	332505.2	31.3	7.9 ± 0.2	1.7 ± 0.5	0.08 ± 0.01			
C_2H	N=4-3, J=9/2-7/2, F= 4-3	349337.5	41.9	7.2 ± 0.2	2.6 ± 0.5	0.10 ± 0.02			
C_2H	N=4-3, J=7/2-5/2, F= 4-3	349399.3	41.9	6.8 ± 0.4	3.7 ± 1.0	0.06 ± 0.01			
CN	N=3-2, J=5/2-3/2, F=7/2-5/2	340031.5	32.6	9.7 ± 1	7.6 ± 3	0.06 ± 0.02			
CN	N=3-2, J=7/2-5/2, F=9/2-7/2	340247.8	32.7	7.7 ± 0.2	1.9 ± 0.4	0.23 ± 0.03			
HDCO	5(1,4)-4(1,3)	335096.8	56.2	7.6 ± 0.1	1.8 ± 0.3	0.17 ± 0.02			
HDCO	6(1,6)-5(1,5)	369763.5	70.1	7.1 ± 0.2	1.7 ± 0.6	0.13 ± 0.03			
D_2CO	6(0,6)-5(0,5)	342522.1	58.1	7.8 ± 0.2	1.6 ± 0.4	0.10 ± 0.03			
SiO	8-7	347330.6	75.0	8.6 ± 1.0	30.0 ± 3.0	0.08 ± 0.01			
N_2H^+	4-3	372672.5	44.7	7.3 ± 0.1	3.5 ± 0.4	0.4 ± 0.1	7.3 ± 0.02	1.0 ± 0.1	1.8 ± 0.1

Table A.3. Molecular Line Detections for NGC 1333-IRAS 4C - JCMT data

				Broad	**component**		**Narrow**	**component**	
Molecule	Transition	Rest Frequency (MHz)	E_{up} (K)	V_{lsr} (km s^{-1})	FWHM (km s^{-1})	T_A^* (K)	V_{lsr} (km s^{-1})	FWHM (km s^{-1})	T_A^* (K)
HCN	4-3	354505.5	42.5	8.35 ± 0.06	1.2 ± 0.1	0.21 ± 0.02			
HNC	4-3	362630.3	43.5	8.58 ± 0.05	1.15 ± 0.09	0.42 ± 0.03			
CO	3-2	345796.0	33.2	8.7 ± 0.5	5.1 ± 0.9	2.6 ± 0.4	6.8 ± 0.1	1.3 ± 0.3	4.1 ± 0.9
^{13}CO	3-2	330588.0	31.7	8.2 ± 1.2	1.9 ± 0.1	2.9 ± 0.1			
$C^{17}O$	3-2	337061.1	32.4	8.27 ± 0.02	0.96 ± 0.05	0.69 ± 0.01			
HCO^+	4-3	356734.1	42.8	8.5 ± 0.03	1.52 ± 0.07	0.99 ± 0.04			
$H^{13}CO^+$	4-3	346998.3	41.6	8.44 ± 0.06	1.2 ± 0.1	0.20 ± 0.01			
CS	7-6	342882.8	65.8	8.5 ± 0.1	1.1 ± 0.3	0.35 ± 0.08			
CH_3OH	4(0,4)-3(-1,3)	350687.7	36.3	7.6 ± 0.3	3.4 ± 0.6	0.09 ± 0.01			
H_2CO	5(1,5)-4(1,4)	351768.6	62.4	8.31 ± 0.04	1.3 ± 0.1	0.40 ± 0.03			
H_2CO	5(0,5)-4(0,4)	362736.0	52.3	8.72 ± 0.08	1.4 ± 0.2	0.20 ± 0.02			
DCO^+	5-4	360169.8	51.9	8.4 ± 0.5	0.9 ± 0.5	0.2 ± 0.1			
SO $^3\Sigma$	3(3)-3(2)	339341.5	25.5	8.2 ± 0.3	1.8 ± 0.8	0.09 ± 0.03			
SO $^3\Sigma$	7(8)-6(7)	340714.2	81.2	8.7 ± 0.2	2.0 ± 0.4	0.06 ± 0.01			
SO $^3\Sigma$	8(8)-7(7)	344310.6	87.5	8.8 ± 0.8	0.8 ± 1.8	0.1 ± 0.2			
SO $^3\Sigma$	9(8)-8(7)	346528.5	78.8	8.6 ± 0.1	1.9 ± 0.1	0.11 ± 0.01			
C_2H	N=4-3, J=9/2-7/2, F= 4-3	349337.5	41.9	7.9 ± 0.2	1.9 ± 0.4	0.21 ± 0.03			
C_2H	N=4-3, J=7/2-5/2, F= 4-3	349399.3	41.9	7.7 ± 0.1	1.9 ± 0.3	0.17 ± 0.02			
CN	N=3-2, J=5/2-3/2, F=7/2-5/2	340031.5	32.6	9.2 ± 0.2	2.4 ± 0.5	0.09 ± 0.01			
CN	N=3-2, J=7/2-5/2, F=9/2-7/2	340247.8	32.7	8.7 ± 0.1	1.4 ± 0.3	0.22 ± 0.04			
N_2H^+	4-3	372672.5	44.7	8.1 ± 0.1	0.9 ± 0.2	0.55 ± 0.05			
H_2D^+	1(1,0)-1(1,1)	372421.4	104.2	8.4 ± 1.1	1.7 ± 1.2	0.08 ± 0.03			